JARRAD ALLERY – 32892911

MURDOCH UNIVERSITY

.

Feasibility Analysis and Simulation of Reverse Electrodialysis for the Regeneration of Power in Desalination Plants

Supervised by:

A/Prof Philip A. Schneider

Abstract

This document presents a multi-faceted parametric review on the reverse electrodialysis process regarding ideal and real feed solutions. A hybrid forward osmosis - reverse electrodialysis model is presented for the optimal utilisation of desalination brine effluent for electrical power generation. The power generated is recommended to offset the high energy requirements of seawater reverse osmosis desalination due to relative proximity of brine. The proposed large scale reverse electrodialysis plant has the potential to minimise both capital and operating expenditure of an up-scaled system while maximising net power output. A multi-variable optimisation of the process is achieved using the simulation model derived within the study, concluding with a 10.3% reduction in the specific energy consumption of Perth's Seawater Desalination Plant located in Kwinana when utilising a series-parallel arrangement of reverse electrodialysis units. However, the model is not specific to a Western Australian context and can be used wherever an opportunity for salinity gradient power generation exists.

ACKNOWLEDGEMENTS

My family/friends for their words of encouragement and my supervisor Phil for being a friend and mentor in this assignment. Absolutely couldn't have done it without him and his ability to deconstruct and rebuild concepts in his own way, as to explain them to me. A genuine and rare teacher.

DECLARATION OF CONFLICTING INTERESTS

The author declares that there is no known personal relations and/or financial motivation that would bias the results of the study.

TABLE OF CONTENTS

TABLE OF FIGURES

TABLE OF TABLES

1.0 INTRODUCTION & BACKGROUND

As the effects of climate change are compounded with a steady rate of population growth and the continued emission of greenhouse gases, water scarcity, in regard to quality and quantity, is becoming a prevalent issue globally (van Vliet et al., 2021). The results, of which, are increasingly fewer opportunities for conventional surface water harvesting methods to be practiced sustainably as the climate dries, depicted in Figure 1 (Hofste et al., 2019).
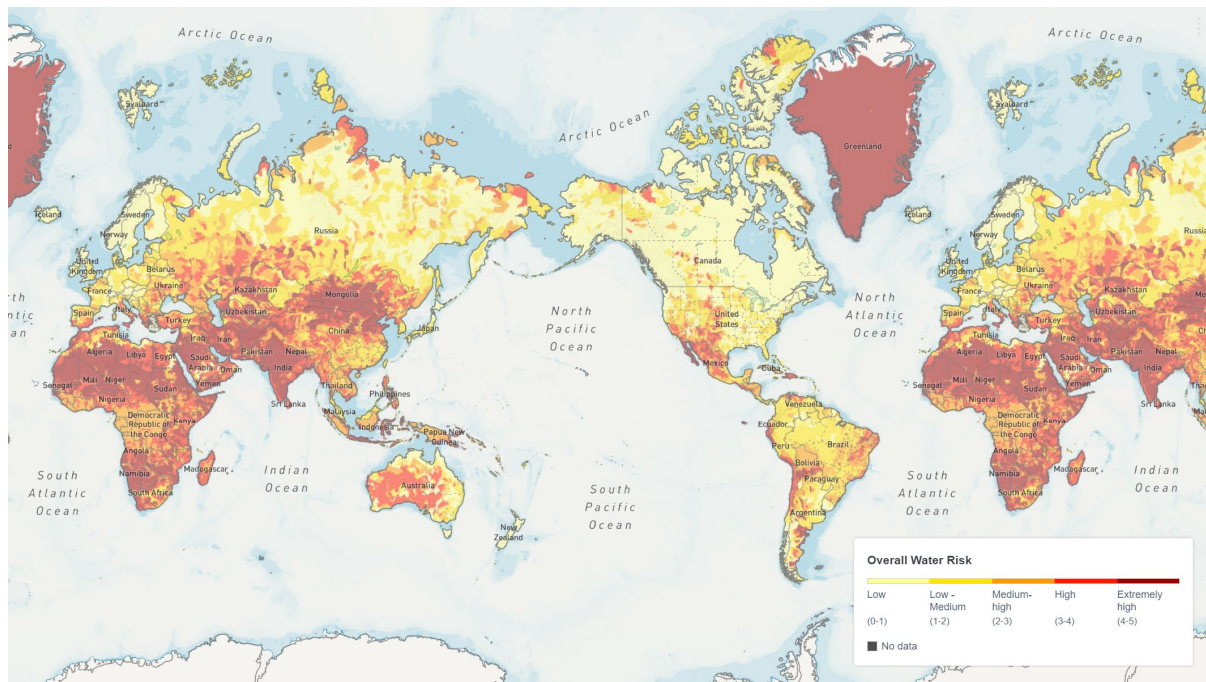
Figure 1. Global Water Risk Heat Map (Hofste et al., 2019).

Clean water is a necessity for human survival and is a requirement for sustainable development under the United Nations' 6th Sustainable Development Goal (United Nations, 2015). Water scarcity is a prevalent and urgent issue that currently threatens 2.1 billion people, many of whom do not have reliable access to safe drinking water (Li & Yang, 2021). As such, alternative sources of freshwater production, such as solar desalination, treated wastewater reuse, capacitive deionisation, and reverse osmosis aim to alleviate this issue. However, they are constrained by technical and economic aspects such as high power requirements, low conversion efficiencies and high costs of production compared to surface and ground water harvesting as depicted in Table 1 (van Vliet et al., 2021). Seawater reverse osmosis (SWRO) desalination plants are employed globally to supplement dwindling fresh water sources (Mekonnen & Hoekstra, 2016), however, the energy demands of the process can be up to 70% of the total cost of desalinated water production (Stover, 2007). The vast majority of SWRO plants are dependent on fossil fuels for their power requirements. Large scale operations require an average specific energy consumption (SEC) of 5.5 kWh m^{-3} at a 50% recovery rate as displayed in

Table 1 (Nassrullah et al., 2020; Schiermeier, 2008). There are pilot plants that have reached SEC of 1.80 kWh/m^3 which is approaching the thermodynamic limit of 1.07 kWh m^{-3} at 50% recovery, but the technology is currently not scalable due to manufacturing limitations (Elimelech & Phillip, 2011; Kim et al., 2019). A dominant view from researchers is that seawater desalination will become one of the few feasible options of supplying potable fresh water to the population if the current 'business as usual' method of economic growth is maintained, as displayed in Figure 2 (Charcosset et al., 2009; Jones et al., 2019). Seawater desalination can be accomplished through a plethora of different techniques such as Reverse osmosis (RO), Multi-stage flash (MSF), Multi-effect distillation (MED) and electrodialysis (ED). This study will be focussed on subsidising the energy requirements of the membrane based RO desalination method as it is the most common.

Water Source	Average SEC (kWh m^{-3})
Surface water	0.37
Ground water	0.48
Treated wastewater	0.75
Wastewater reuse	1.75
Seawater	5.54

Table 1. Global Average SEC of Producing 1m^3 of Drinking Water from Varying Sources. Reproduced from (Nassrullah et al., 2020). SEC: Specific Energy Consumption.
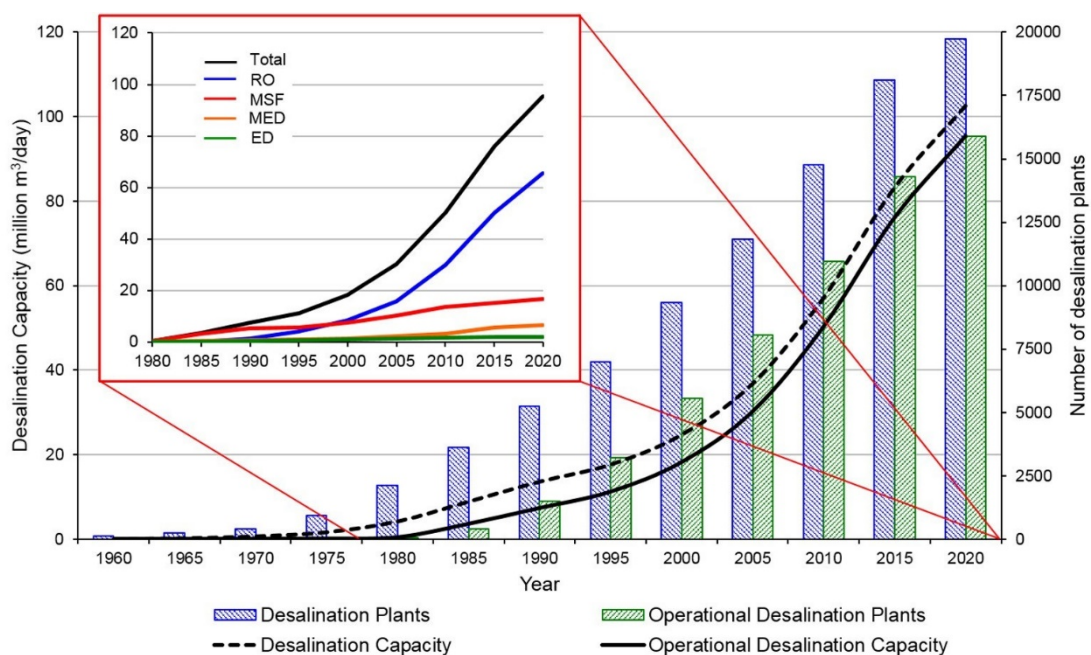
Figure 2. Trends in Global Desalination Capacity (Jones et al., 2019).

1.1 RESEARCH QUESTION

This study aims to evaluate the application of reverse electrodialysis (RED) to determine if meaningful power can be regenerated through the utilisation of SWRO brine that is generally discarded to the ocean. RED is a largely underdeveloped method of non-polluting electrochemical renewable energy production.

1.2 MOTIVATION FOR STUDY

From travelling through India and Southeast Asia, it has been made evident that an extreme prevalence of impaired drinking water sources exist for both highly and sparsely populated developing regions, creating numerous challenges in the generation and distribution of fresh water. These experiences motivated me to be a part of the solution in terms of optimising potable drinking water production. As a large proportion of drinking water in the future will be derived from SWRO plants, the possibility of offsetting the energy requirements is of interest. As someone living in a relatively privileged area, Western Australia, wherein 50% of our freshwater demand is met by desalination, I understand that this is not an issue specific to 3rd world countries but something that challenges the world as a whole.

1.3 METHODOLOGY

This study has only included relevant and good quality research designs which produce repeatable outcomes. Listed are the sources and criteria that each paper used was required to agree with in order to be included in the study. As a person from an engineering discipline, I deal in objectivity, the perspective had to be quantitative, measurable, observable, repeatable. Which was achieved by utilising secondary data analysis techniques to verify existing research to hopefully provide a unique perspective, progressing the technology in question. Secondary research involves interrogating and considering data that has been collected and displayed by a researcher in the past.

I have chosen data from these areas:

- Peer reviewed, professional journals
- Textbooks
- Government documents
- Technical publications
- Current research

I have excluded non peer reviewed journal articles or unsubstantiated internet publications. I have chosen secondary data specific to my area of interest as to inform my study with the best possible quality breadth and depth of relevant research to create a balanced view. I have chosen secondary research because it is cost effective, and I am time constrained, I do not have the means to conduct independent experiments. I do not have to pay for transport, office space, equipment, or staff. Furthermore, I have a large scope of data from which to choose, which has enabled me to explore trends and changes over time. Disadvantages of using secondary data is finding data that specifically fits with my stated aim. Data may be in a different format to what I may be experienced with. I have a lack of control over the quality of the data and must be diligent in making assessments as to the quality of each document to the best of my ability as a beginning researcher. I've chosen each data set for its congruency with its stated research aims, the credentials of the institution producing the data and its relevancy. I must be reflexive to the extent I understand my own bias. My bias is that I want this technology to be feasible in both technical and economic aspects using current membrane manufacturing methods. Therefore, as a means of reducing my bias I have developed a standard set of questions with which to interrogate the data. The questions are set out below.

Evaluation of secondary data:

- What is the aim of the original study?
- Who collected the data?
- Which measures were employed?
- When were the data collected?
- What methodology was utilised?
- What are the outcomes?
- How do they compare with similar studies?
- Are there un-controlled variables?
- Are they like for like?
    - If not, how do I account for differences?
    - Are they still valid to be compared?
    - Is there disagreement and/or anomalies?

These questions aim to mitigate any bias I may have towards the literature. I am also aware of p-hacking and cherry picking and strive to keep my findings un-biased.

1.4 AIMS AND OBJECTIVES

The aim of this study is to explore reverse electrodialysis, which promises to be a renewable, sustainable, and clean (zero emissions) form of salinity gradient power generation that uses an essentially free fuel (salt water). This evaluation is undertaken to determine if RED, in its current technological state, can generate net positive energy when harnessing the salinity gradient potential from effluent water streams of differing salt concentrations involved with SWRO desalination and Wastewater treatment. The project objectives include:

- Assessing the current viability of energy generation using SWRO brine effluent and seawater

- Assessing effects on the RED process when the high concentration solution (brine) is paired with seawater.

- Assessing effects on the RED process when the low concentration solution (seawater) is diluted further through forward osmosis (FO) with treated wastewater before RED.

- Assessing the net power generation of the RED process using current & available membrane technology.

2.0 LITERATURE REVIEW

2.1 SEAWATER REVERSE OSMOSIS (SWRO)

Due to nearly half of the world's population living less than 100km from an ocean, SWRO remains the most economical form of desalination, however, energy consumption generally makes up 50% of operational expenditure (OPEX) of the process as shown in Figure 3. Within that total energy consumption bracket roughly 70% of the specific energy consumption (SEC) is derived from pumping saltwater through polyamide RO membranes at pressures up to 80 bar, which is in excess of 1000psi (Verbeke et al., 2017). So, while it is important to work out how to improve the membrane performance characteristics, other clever process optimisations exist, such as pressure exchange modules. Displayed as the yellow cylinders in Figure 3, these devices can recover energy from the pressurised concentrated effluent leaving the desalination plant and re-implement that hydraulic energy back into the feed stream at 95% efficiency. Other examples of process optimisation techniques include operating all supply, booster and second pass pumps on variable frequency drivers. This allows for autonomous regulation of flow rates within the system, subsequently boosting efficiency (Sanz et al., 2007). These are just examples of how it is possible to make desalination more

efficient by looking outside of membrane operations, which is what this study hopes to achieve to a degree.
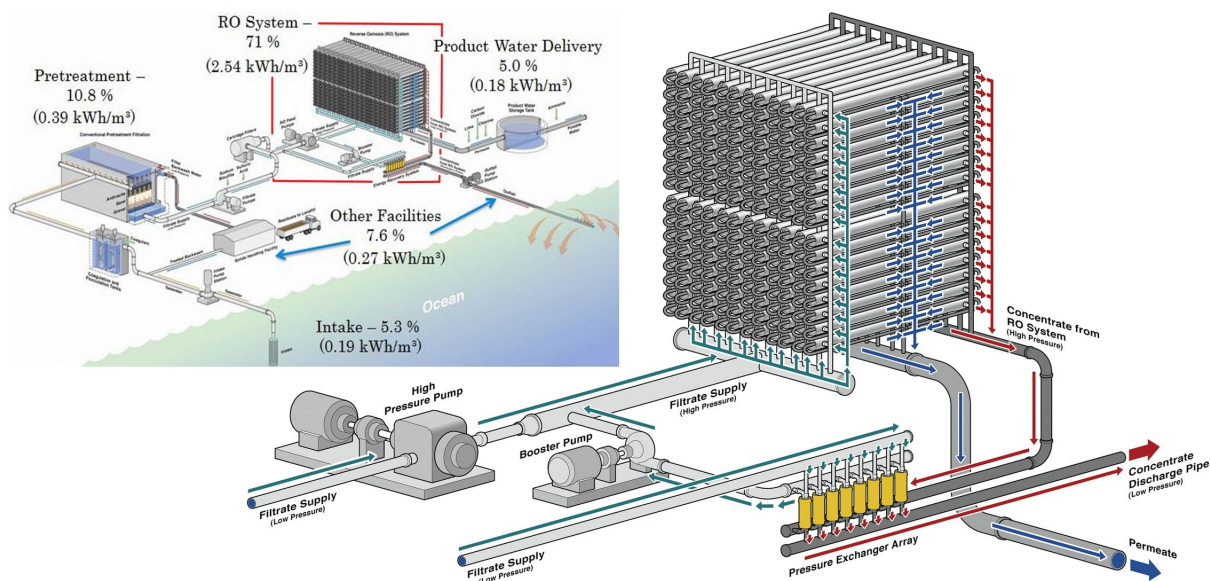
Figure 3. Conventional Desalination Process and SEC (kWh m⁻³) Breakdown (Voutchkov, 2018).

The laws of thermodynamics limit an average cubic metre of seawater at standard temperature and pressure (S.T.P) to require 0.78kWh (at 0% recovery) to turn it into potable drinking water (Amy et al., 2017). This is the absolute minimum amount of energy required and it assumes 100% mechanical efficiency of the system, which isn't possible as desalination plants are not reversible thermodynamic processes (Rabiee et al., 2019). The practical sustainable desalination zone as defined by the UN's COP21 goal is 25-30% of the thermodynamic limit, which will help to limit the global temperature increase to 2 degrees Celsius above pre-industrial levels before 2100 (Shahzad et al., 2017). A lot of effort has gone into developing new processes for both membrane and thermal desalination to move towards this goal. The Aquaporin membrane uses proteins found in biological cells to boost the permeability of these membranes by a whole magnitude and in 2003 won Peter Agre the Nobel Prize in chemistry for his discovery (Agre, 2006). However, production methods for membranes such as these are not economically viable at present.

The advancement of SWRO is constrained by the large SEC of the process. Hence, the most favourable way for this technology to progress is to minimise the SEC. This can be achieved through optimising SWRO factors that are related to the SEC such as feed stream conditions, target stream parameters (quality/quantity), and operational efficiencies (energy recovery devices and pumps) (Kim et al., 2019). In comparison to the conventional treatment of surface and ground water sources, of which requires 0.3-0.5 kWh/m³ (Kim et al., 2019; Voutchkov, 2018; Wakeel et al., 2016) the theoretical thermodynamic minimum specific energy requirement to desalinate seawater at a 50% recovery rate with total dissolved solids of 35000 mg/L, is 1.07kWh/m³ (Kim et al., 2019; McGovern,

2014; Park et al., 2018; Voutchkov, 2018). Operational SWRO plants require a much greater SEC than the thermodynamic minimum at 4-6 kWh/m^3 where the RO process accounts for up to 70% of this energy demand (Voutchkov, 2018). It is for this reason that the current bias of water sourcing leans towards surface and ground water harvesting as opposed to desalination.

The utilisation of SWRO is inevitable for areas that only have access to saline sources for potable water generation such as the Middle East and North Africa, of which are increasing demand for SWRO water to use in both agriculture and human consumption as water scarcity grows (Ghaffour, 2009). It is forecasted that surface water sources in these sensitive areas will not stabilise in the future with current trends (Ramanathan & Feng, 2009). Potable water from SWRO comes at a higher price in terms of energy as shown in Table 1. This energy is generally generated by burning fossil fuels, hence further contributing to climate change through the continual emission of greenhouse gases into the atmosphere. Fundamentally, strategies need to be devised in order to approach the thermodynamic limit of SWRO, as to minimise the process' carbon footprint and optimise the SEC of potable water production.
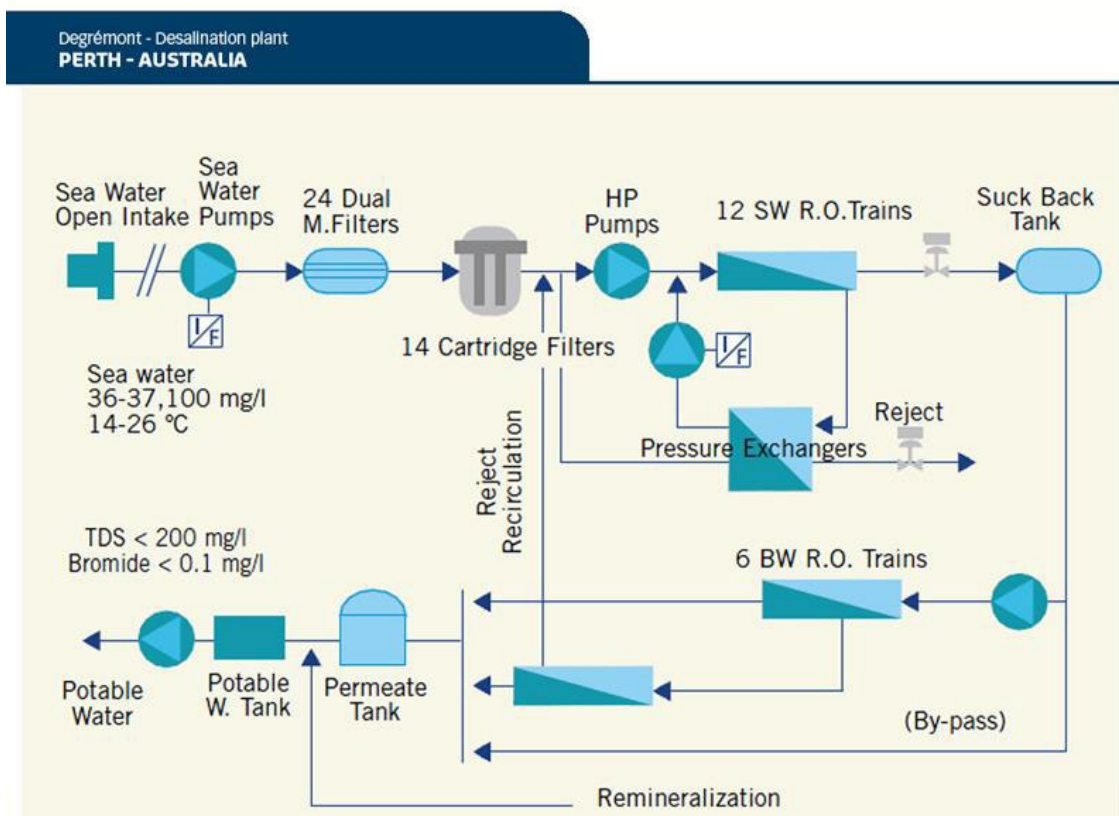
Figure 4. Perth SWRO Desalination Plant Setup. (Mickley et al., 2016).

SWRO remains the most economical form of desalination, but power consumption generally makes up 50% of OPEX, the process of which is shown in Figure 4. This is in terms of electrical power consumption within the plant processes, it does not account for the embodied energy of chemicals required for chlorination/coagulation/flocculation/antiscalant/remineralisation/fluoride dosing/anti-

biofouling solutions for the membranes that are necessary for the beneficiation stage of raw feed water for SWRO systems, such as (Younos, 2005):

- Sodium hypochlorite (NaOCl), otherwise known as free chlorine, which is used to mitigate biological build-up on the membranes.
- Ferric and/or aluminium chloride ($FeCl_3$/$AlCl_3$) are employed as disinfectants for the flocculation stage and the entrapment of suspended solids in solution.
- Sulfuric and/or hydrochloric acid (H_2SO_4/HCl) are utilised to control the pH of the feed streams.
- Anti-scalants such as sodium hexameta phosphate (($NaPO_3)_6$), also known as SHMP, are used to prevent mineral coatings and corrosion deposits forming in the pipes and membranes.
- In order to neutralise any remaining free chlorine in the seawater, sodium bisulphate ($NaHSO_4$) is employed.
- Other deposits, such as carbonate, are dissolved using acid solutions ($C_{10}H_{16}N_2O_8$), also known as EDTA – ethylenediaminetetraacetic acid.
- Other acids are used three or four times annually to flush the membranes. These include citric acid ($C_6H_8O_7$) and sodium polyphosphate (Na_3PO_4) in conjunction with EDTA.

The basic operation of a desalination plant, the Perth Seawater Desalination Plant (PSDP) in this case, is as follows (Mickley et al., 2016):

I. Seawater intake uses an electric pump to bring influent seawater to a dual media filter and then a secondary pump is utilised to transport that water to cartridge filters.

II. From the cartridge filters a low-pressure feed booster pump sends the filtered sea water to
   a. The series of high pressure pumps that drive seawater through the RO membranes.
   b. The energy recovery devices to enable the return of the hydraulic piston that previously extracted energy from the brine (concentrate stream). This process drastically reduces the energy demand of the system as it recovers energy from a stream that was, in the past, pumped back to the ocean carrying enormous hydraulic energy.

III. [1st pass] The series of high pressure pumps reverse the osmosis phenomenon by hydraulically forcing seawater through a bank of semipermeable membranes in order to separate the dissolved salts in solution. This is the most energy intensive part of the SWRO system as an enormous amount of energy is required to bring the feed water up to 80 bar (~1160 Psi).
   a. The rejected brine stream from this is still under enormous pressure and is sent to the energy recovery device (ERD) to pressurise hydraulic pistons that then feed

pressurised filtered seawater to a ERD booster pump. This then sends water to the start of the membrane bank to be integrated with the high pressure pump streams.

IV.   [2nd pass] The diluted seawater is again sent to a high pressure pump to be sent to a second bank of RO membranes to finally remove all the ions from solution, resulting in pure H_2O. Although less energy intensive than the first pass, the second pass still requires a large amount of energy.

      a.   The rejected brine from these membranes is sent to the ocean.

      b.   The product stream is sent to a surge tank.

V.   From the surge tank an electric transfer pump sends the water to a permeate tank and subsequently, from another transfer pump to the scheme water mains or a potable water tank.

The largest source of electricity demand within the system are the first and second pass high pressure pumps, so they subsequently offer the largest opportunities for savings. There are opportunities to optimise plant efficiency through such methods like ERD's and pump design by tailoring them specifically to RO applications but another interesting way to reduce power requirements for an RO plant is by diluting the seawater initially using forward osmosis (FO), described further in section 2.8. There are other low salinity feed solutions apart from river water that otherwise get pumped into the sea, such as treated wastewater (TWW). Hence, by using TWW as a feed solution, it is possible to recover 'fresh' water that would otherwise be lost to the ocean. In this case, instead of having pure seawater that requires greater hydraulic pressures to drive through RO membranes due to higher ionic concentration, a more dilute solution is available that requires less energy to produce the same volume of drinking water. This process would reduce the overall energy demand and subsequent OPEX of the RO plant. Unfortunately, a western stigma exists about using TWW, also there is an implication that brand new sets of membrane biofouling, pumping/plumbing, health/safety risk characteristics are introduced to the RO plant as there are only a few membranes separating TWW from the potable water being produced. A safer alternative would be to simply generate electrical power for the SWRO plant by utilising salinity gradient power.

2.2 SALINITY GRADIENT POWER (SGP)

Salinity gradient power (SGP) utilises membrane conversion techniques, such as Pressure Retarded Osmosis (PRO) and Reverse Electrodialysis (RED), in which the latter utilises a chemical potential difference that is generated through the mixing of two electrolyte solutions of varying salinities (Ramon et al., 2011). When these water streams, one of a relatively higher salt concentration than the other mix, energy is discharged as a result of the difference in chemical potential between the two solutions. This chemical mechanism causes an increase to the entropy of the system in an irreversible

and spontaneous way and provides an opportunity to generate renewable power (Pawlowski et al., 2016). Fresh/brackish river systems drain into oceans all over the planet, when this happens both streams mix spontaneously and irreversibly. If, however, the mixing occurs in a controlled and reversible manner, otherwise wasted work can be harnessed from an inevitable scenario (Isaacs & Schmitt, 1980). SGP can therefore be considered an entirely renewable and sustainable opportunity for energy production (Pawlowski et al., 2016). Table 2 depicts a comparison of SGP with other energy conversion methods.

Energy Conversion Systems	GHGs [g CO_2-e /kWh]	Electricity Price [USD/kWh]	EROI	Energy Conversion Efficiency [%]
Photovoltaic	90	0.24	1.6-6.8	4-22
Wind	25	0.07	18	24-54
Hydro	41	0.05	>100	>90
Geothermal	170	0.07	N/A	10-20
Coal	1004	0.042	80	32-45
Gas	543	0.048	10	45-53
RED	<10	0.10	7	34-40
PRO	<10	0.065-0.13	6.7	44

Table 2. RED and PRO in comparison to other energy sources. Reproduced from (Zoungrana & Çakmakci, 2021). EROI: Energy return on investment.

On average, for every cubic metre of river discharge mixed with sea water, thermodynamic models predict 1.2 MJ can be obtained (Kuleszo et al., 2010; Quak, 2009), the relationship is depicted in Figure 5.
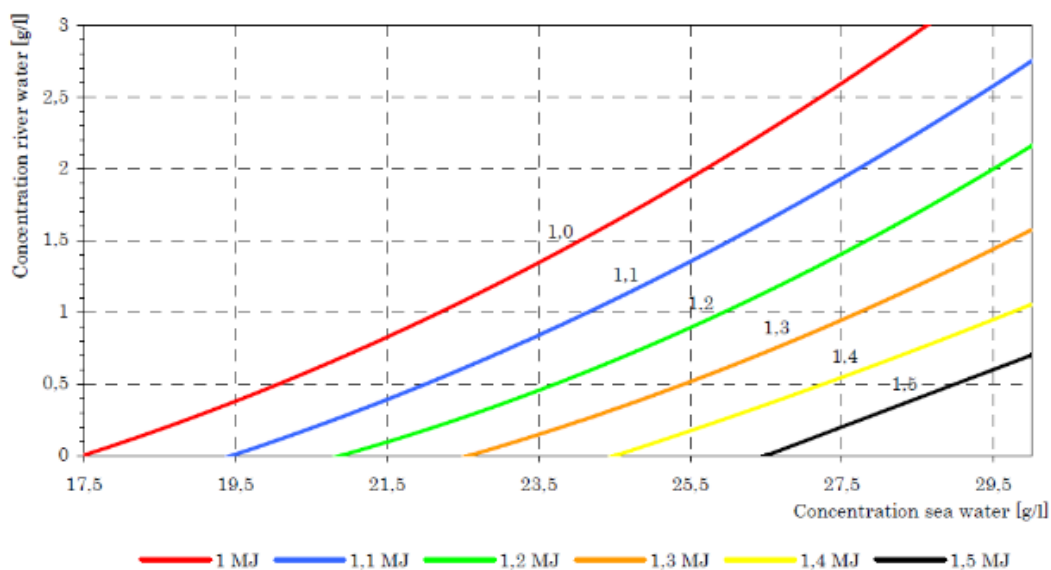
Figure 5. Theoretically available Gibbs Free Energy from thermodynamic modelling of 1m³ of ocean water homogenously mixed with 1m³ of river water (Post et al., 2007).

SGP is predicted to be one of the highest sources of energy in a marine based environment, second only to offshore wind power (Zoungrana & Çakmakci, 2021). Figure 6 depicts the theoretical chemical potential for energy generation is 984 GW or 8619.84 TWh/year globally. This translates to roughly 18.2% of global primary energy consumption in 2018 (Isaacs & Schmitt, 1980; Zoungrana & Çakmakci, 2021). When factors such as suitable plant location, average river discharge rates and extraction/capacity factors are taken into consideration, estimates theorise 3-15% of the world's power demands may still be met (Alvarez-Silva et al., 2016).
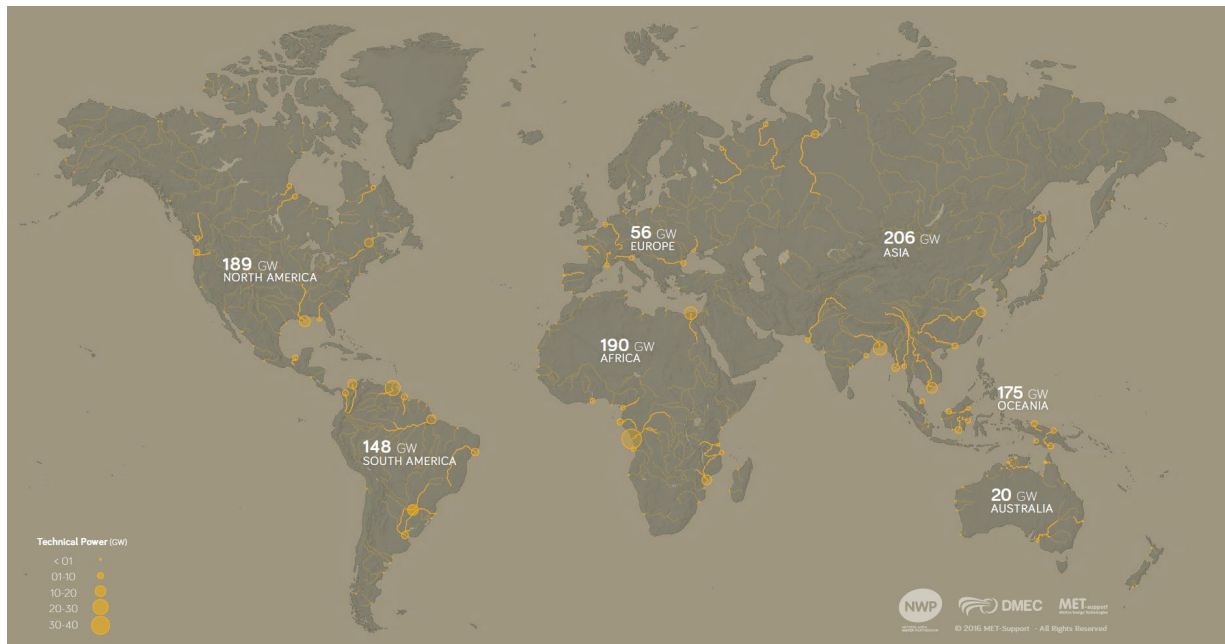
Figure 6. Global Map of Potential Salinity Gradient Power (REDstack, 2016)

As opposed to conventional river/sea interfaces for salinity gradients, hybrid systems can be employed that utilise highly saline sources for the concentrated feed for SGP production. These may include inland lakes that have been subject to groundwater salinity, saline aquifers/wastewater streams, industrial mining pits and desalination brines (Helfer et al., 2013; Jones & Finley, 2003; Kempener & Neumann, 2014; Merz et al., 2012; Neumann, 2012). A summary of the data from (Logan & Elimelech, 2012) depicts the osmotic pressure of various sources of highly saline sources. This can be regarded as a visual representation of the power generation capacity of different saline sources as concentration and osmotic pressure are directly related, the higher the concentration the larger the chemical potential is theoretically possible as depicted in Eqn (5) (Pawlowski et al., 2016). A cubic metre of brine (5M) mixed with a cubic metre of river water (0.01M) can theoretically produce 16 MJ of power as well as increasing ecological welfare through the dilution of SWRO brine that is discharged into marine environments (Post et al., 2007).
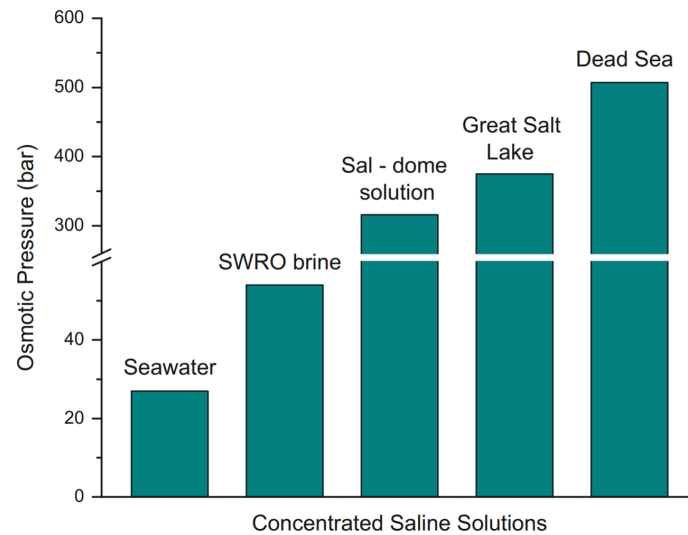
Figure 7. Varying sources of saline/hypersaline solutions and respective osmotic pressures (SWRO – Seawater Reverse Osmosis) (Logan & Elimelech, 2012; Pawlowski et al., 2016).

2.3 REVERSE ELECTRODIALYSIS (RED)

A RED system employs multiple ion exchange membranes (IEM) (anion/cation permeable) in a bank, sandwiched between an anode and cathode. The channels between the membranes co-currently flow with relatively fresh and saline solution. Osmotic pressure drives the free ions in solution in opposite directions due to the selective nature of the membranes, wherein the negatively charged ions will pass through anion-exchange membranes (AEM) towards the anode (oxidation) and the positively charged will move through cation-exchange membranes (CEM) towards to the cathode (reduction) (Lacey, 1980). As there is a negative and positive charge (ionic flux) at opposite ends of the membrane, a direct electrical current can be generated when an external circuit is created, thus providing power to whatever load is applied to the circuit as demonstrated in Figure 8 (Telesh & Khlebovich, 2010; Turek & Bandura, 2007). The salinity gradient between these membranes generates a potential difference (80 mV for river/sea water on average) (Ramon et al., 2011), which is known as the 'membrane potential'. Practical RED systems use thousands of such membranes in a 'stack' (electro-chemical cell), and the final potential difference of the stack is the sum of membrane potentials (E) (Telesh & Khlebovich, 2010).

$$P = E \times I$$

(1)

The power (P) generated from the stack is in watts. E is the potential difference of the stack in volts and I is the external current generated in amperes, of which is derived from the sum of the average current density along the length of the cell and the area of the membrane (Ortiz-Imedio et al., 2019).

The metric used most frequently in literature to determine the performance of a RED stack is the net power density per membrane cell pair (W m^{-2} cp).

$$P_{net\ density} = P_{gross\ density} - \frac{P_{pumping}}{2 \cdot N \cdot A_m}$$

(2)

Where A_m is the surface area of a single membrane and N is total number of cell pairs (CP) within the stack (Vermaas et al., 2012; Vermaas et al., 2011a). Where a cell pair is the parallel configuration of the high and low concentration feed streams separated by an IEM. When hydrodynamic conditions are kept the same in both the high and low concentration compartments (flow rate/temperature), the power required for pumping can be derived from the following (Pawlowski et al., 2016).

$$P_{pumping} = (\Delta p_{LC} \cdot Q_{LC}) + (\Delta p_{HC} \cdot Q_{HC})$$

(3)

Where Q is the flow rate (m^3 s^{-1}) of either the high/low concentrate solutions and $\Delta p_{LC/HC}$ is the drop in pressure between the influent and effluent in respect to low or high concentration streams in pascals. This is the sum of partial pressure drops that occur throughout the RED system, including those in the electrode rinse solution (ERS). The ERS pressure drops become negligible in large scale systems (N>200) (Strathmann, 2010). The gross power density produced from a RED stack is dependent on the open circuit voltage (OCV) which is the voltage produced when there is no external load/resistance. Maximum gross power density generated when the resistance within the stack is equal to the external resistance (Veerman et al., 2009; Veerman et al., 2008; Veerman et al., 2010). In such a circumstance:

$$P_{gross\ density} = \frac{OCV^2}{4 \cdot R_i}$$

(4)

OCV represents the maximum power a RED stack can generate. It is the sum of each individual membrane chemical potential difference, of which is determined by the activity/concentration ($\gamma \cdot$C) ratios between concentrated and dilute feed streams (Pawlowski et al., 2016).

$$OCV = 2N \cdot \alpha \cdot \frac{R \cdot T}{F} \cdot \ln\left(\frac{\gamma_{HC} \cdot C_{HC}}{\gamma_{LC} \cdot C_{LC}}\right)$$

(5)

The ERS is composed of an aqueous fluid that has the capacity to maintain a balance of anions and cations in the combined anolyte and catholyte solution through a homogenous charge transfer reaction (Veerman et al., 2010). Depending on which type of membrane is utilised as the first and last membrane in the stack (must be the same, i.e. both AEM or CEM) will influence which ion is

responsible for electron transportation (either Na^+ or Cl^-) and will determine which electrode, at opposite ends of the stack, is the anode or cathode, subsequently converting the ionic flux into electrical current via the redox reaction enabled by the ERS as demonstrated in Figure 8. The composition of the ERS can also mitigate gas formation on the electrodes and provide a uniform charge balance, subsequently maximising the system's performance (Benneker et al., 2018). Stable solutions such as a mixture of iron hexacyanoferrate ($K_3Fe[(CN)_6]^{4-}$ / $K_4Fe[(CN)_6]^{4-}$) and NaCl as a supporting electrolyte, are employed due to the optimal reversible-redox capacity under process conditions. It is recommended that exposure of photons and oxygen is negated to minimise the decomposition of the redox couple (Scialdone et al., 2012). It is imperative that the outer IEMs are of the same ion-selectivity, both CEM or AEM for example (Veerman et al., 2010). This is done so that the ionic charge transport from the feed stream to the ERS is done exclusively by Cl^- or Na^+ such that:

$$[Fe(Cn)_6]^{3-} + e \rightleftharpoons [Fe(Cn)_6]^{4-}$$

(6)
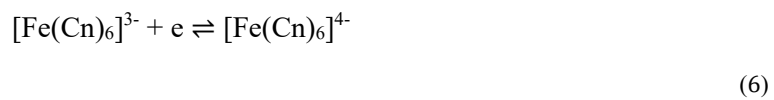
In the case of Figure 8, positive Na^+ ions migrate into the ERS. In this way a reversible redox couple is maintained in the recirculation system which can mitigate short-circuiting of the RED stack, as the potential difference required for the reduction of the electrolyte on the cathode is counteracted by the oxidation at the anode, thus maintaining electro-neutrality (Veerman et al., 2010).
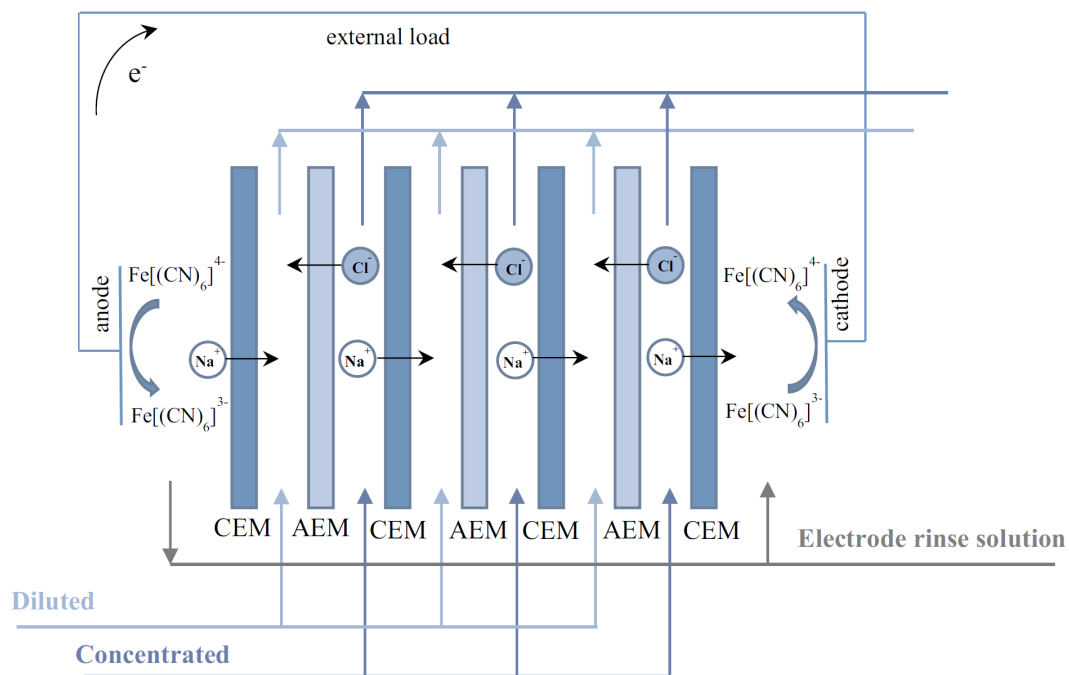
Figure 8. Reverse Electrodialysis Stack Diagram (Ortiz-Imedio et al., 2019)

The ideal/maximum theoretically available potential refers to the Gibbs free energy of mixing. Assuming 100% thermodynamic efficiency, the chemical potential as a function of the concentration

gradient, through reverse electrodialysis, realised under a reversible reaction, follows Eqn. (7) (M Tedesco et al., 2016).

$$P_{\Delta Gmix} = 2RT\left(Q_{LOW}C_{LOW,in}\ ln\frac{\gamma_{LOW,in}C_{LOW,in}}{\gamma_{eq}C_{eq}} + Q_{HIGH}C_{High,in}\ ln\frac{\gamma_{HIGH,in}C_{HIGH,in}}{\gamma_{eq}C_{eq}}\right)$$

(7)

Where Q is the flow rate in $m^3\ s^{-1}$, HIGH & LOW refer to the concentrated and dilute compartments, respectively in mol m^{-3}. C_{eq} is the equilibrium or average concentration in mol m^{-3}, C and γ are the molar concentrations and mean activity coefficients of the respective NaCl feed streams. Activity coefficients can be estimated through the findings of Staples (Staples, 1981) or between [0<C<0.5M] using the Debye Hückel (Veerman et al., 2011) or above [C>1M] using Pitzer equations (Pitzer, 1973; Tedesco et al., 2015). R is the universal gas constant, 8.314 J/(mol·K) and T is the average temperature, in K, of the influent solutions. There have been numerous models developed to estimate mean ionic activity coefficients as demonstrated in Figure 9 and Table 3. The one that comes the closest at replicating experimental data at concentrations beyond 1M is the Pitzer Virial system of equations, which will subsequently be used in the current model due to the high molarities that are associated with the RED process parameters being investigated.
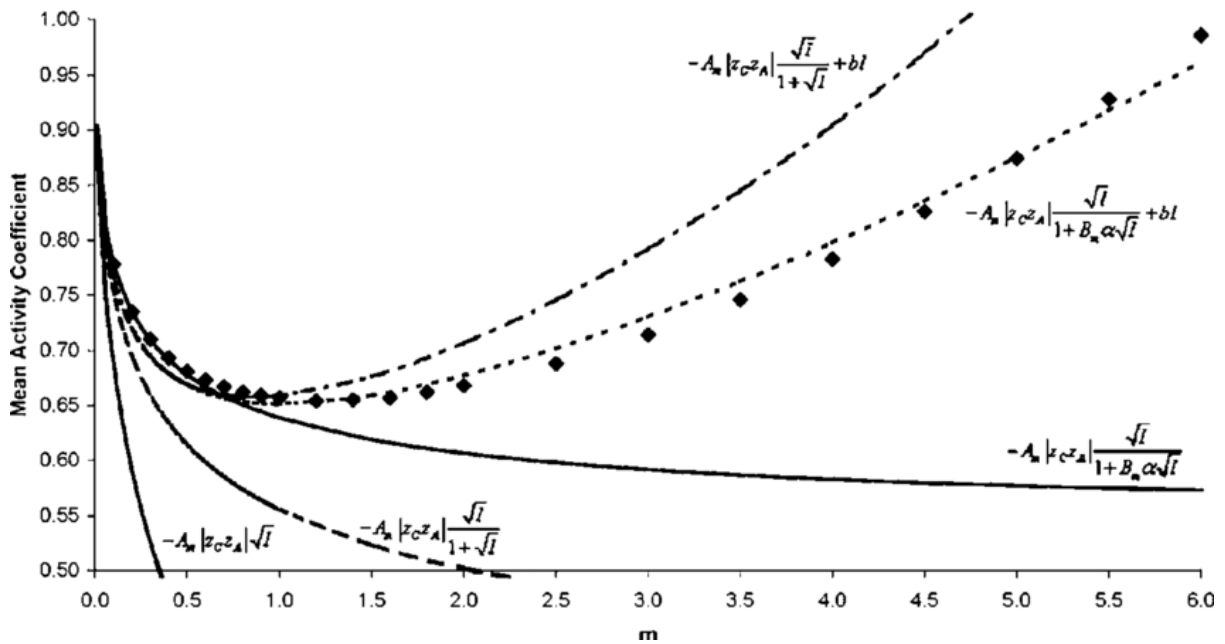
Figure 9. Mean γ vs molality of NaCl at 25°C modelled using various methods (Balomenos et al., 2006). Dots represent the experimental findings of Robinson and Stokes (Robinson & Stokes, 1959).

As 100% thermodynamic efficiency is not realistic, the process efficiency (η_{gross}) is the fraction of actual power generated relative to the theoretically available power described by Eqn. (8).

$$\eta_{gross} = \frac{P}{P_{\Delta Gmix}} \times 100\%$$

(8)

The amount of electrical energy that is practically possible from these stacks is dependent on several factors, such as concentration, composition, and temperature of the two solutions (Katz, 1979). However, the degree to which this energy can be obtained is determined by technical aspects of the system itself, such as internal cell resistance and membrane selectivity, in which the internal resistance is a metric that represents the difficulty ions experience when migrating from the concentrated to dilute solution, and membrane selectivity, which refers to the efficiency of ion passage (Allison, 1995; Katz, 1979). In this regard, the maximum power efficiency (η_p) of the RED process is 50%. Eqn. (9) shows that under ideal conditions in which the stack is operating at maximum power output ($R_i = R_u$), η_p cannot exceed 0.5. The remaining 50% of exergy is lost irreversibly to internal resistances within the stack itself (Veerman et al., 2009).

$$\eta_p = \frac{I^2 R_u}{I^2 R_i + I^2 R_u} = \frac{R_u}{R_i + R_u}$$

(9)

Where R_i and R_u are the total internal and external resistances in the system measured in $\Omega \cdot m^2$. As the complete conversion of Gibbs free energy into electrical energy is not possible, the thermodynamic efficiency of the process is the fraction of power generated by the system relative to the difference in exergy that enters and exits the stack as described by Eqn. (10). The difference in exergy is due to the two feed streams not completely mixing inside the stack, i.e. the ionic flux is not entirely converted into electromotive force and is therefore unused energy (Moreno et al., 2018).

$$\eta_{thermodynamic} = \frac{P}{exergy_{in} - exergy_{out}}$$

(10)

2.4 RED AT LABORATORY SCALE

In a 55 year time frame (1954-2009), only 9 papers were published in scientific journals that describe experimental findings of the RED process with fresh and saline solutions: (Pattle, 1954), (Pattle, 1955), (Kniajev, 2001), (Weinstein & Leitz, 1976), (Audinos, 1983), (Audinos, 1992), (Jagur-Grodzinski & Kramer, 1986), (Turek & Bandura, 2007), (Suda et al., 2007), (Veerman et al., 2008), (Veerman et al., 2009). In the last decade however, the published literature on RED has increased exponentially (Mei & Tang, 2018). Although the aforementioned teams proved the process was more than theoretical, the experimental power densities were low, and the thermodynamic power efficiency was sparsely discussed in literature. In recent times, the understanding and manufacturing capabilities of nanotechnology has improved drastically, and innovative manufacturing processes have enabled the production of perm-selective membranes that far exceed those tested for RED previously (Khatibi et al., 2021). From the 9 mentioned papers, the highest practical power density was achieved by

Veerman et al., 2009 at 1.18 W m^{-2}. Recent advancements include a team (Hsu et al., 2017) that achieved 18.2 W/m^2 using a KCl electrolyte solution and conical shaped steady state nanochannels, depicted in Figure 10. This method was further improved upon by (Khatibi et al., 2021) wherein the nanochannels were internally coated in a polyelectrolyte layer. This addition generated a power density of 51.5 W/m^2. Nearly triple that of the previous maximum in only 4 years. The positive trend of power density improvement with time implies RED could eventually become a competitive source of renewable energy.
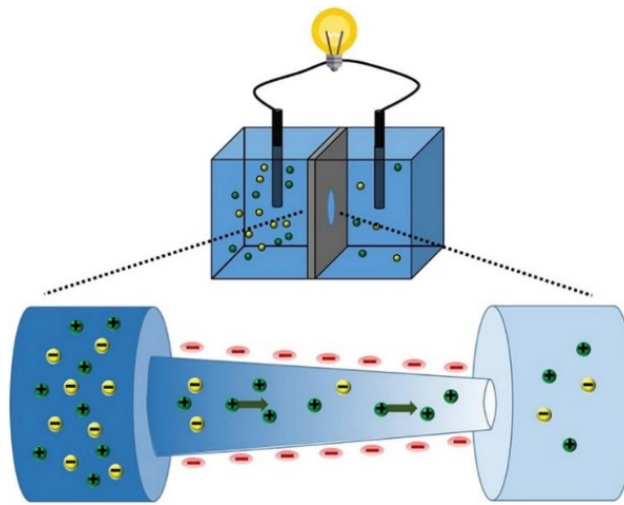
Figure 10. Bare Conical Steady State Nanochannel for RED (Hsu et al., 2017).

2.5 CASE STUDIES

2.5.1 Redstack – Afsluitdijk, Netherlands

The Afsluitdijk (translated: shut-off-dike), is a 32km dam and freeway that joins North Holland to Den Oever in the Netherlands. The construction of the dam itself effectively separated the north (Wadden) sea from the south sea in 1932, subsequently creating the freshwater lake Ijsselmeer (Hakkenes, 2017). Near the middle of the dam lies Breezanddijk Island, a land mass that was deemed an appropriate building location for a RED pilot plant, displayed in Figure 11, due to the relative proximity of salt (0.479 mol/L) and fresh (0.0034 – 0.0086 mol/L) water. The pilot plant was operational in 2014 and had a nominal power generation of 50 kW (Ortiz-Imedio et al., 2019).
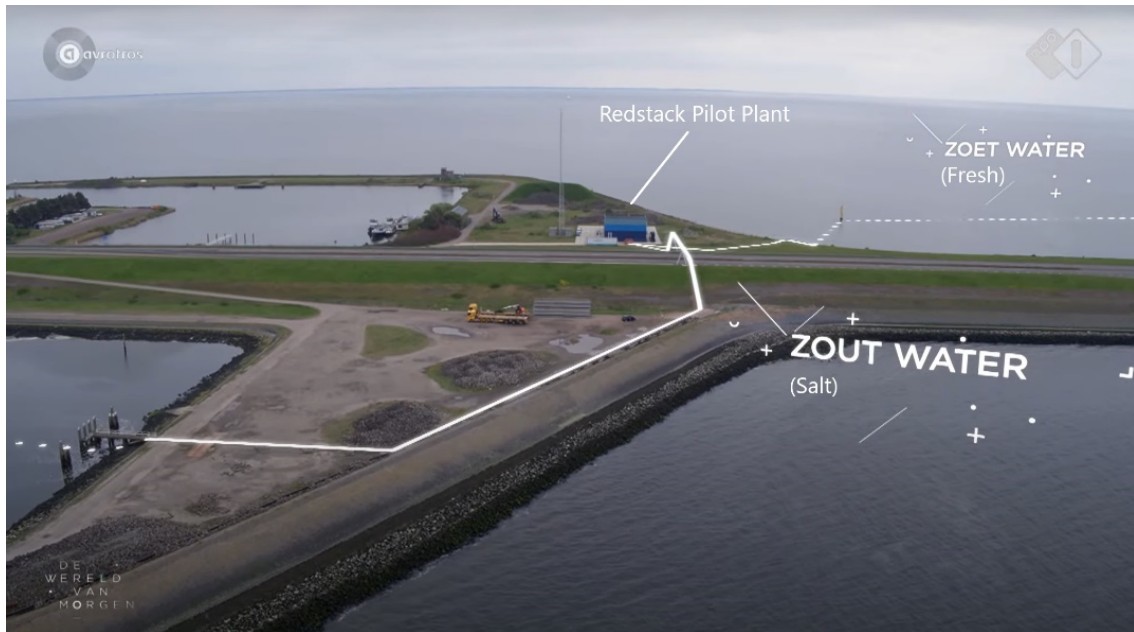
Figure 11. Redstack Pilot Plant on Breezanddijk Island (Avrotros, 2019)

The Redstack pilot plant was developed with the intention of determining the effects that upscaling has on RED systems. Specifically, the effects that larger stack sizes have on process efficiency and power density, as these are critical parameters for the commercialisation of industrial scale RED power plants (Moreno et al., 2018). These effects were studied using 4 separate stacks that employed 50 membranes each. (6×6), (10×10), (22×22) and (44×44) cm^2 membranes were used, respectively, which translated to effective membrane surface areas of 0.36, 1.00, 4.84 & 19.36 m^2.
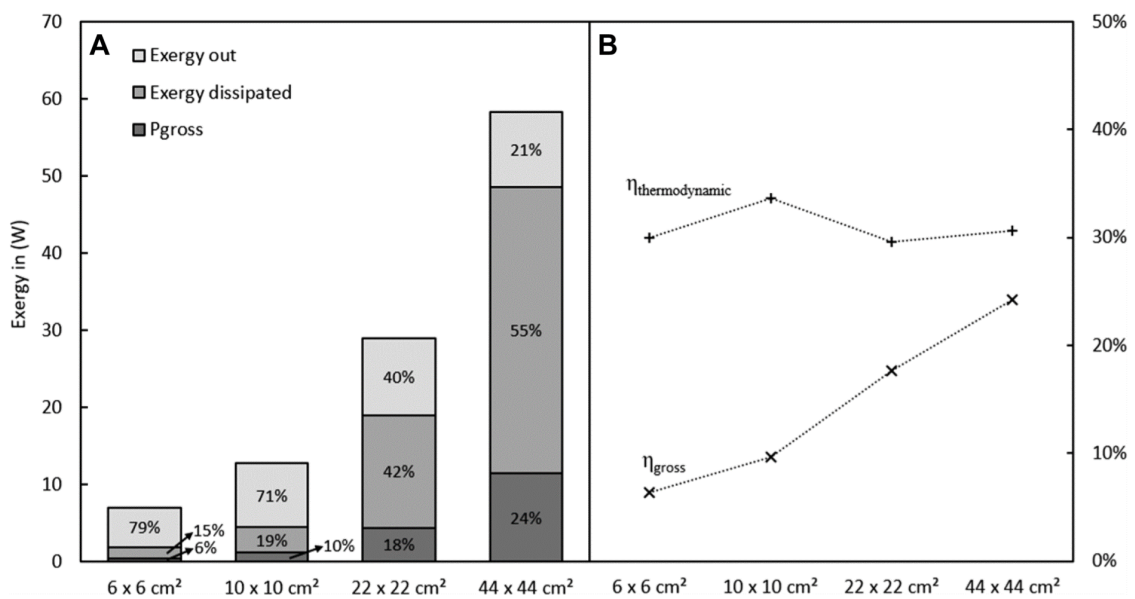
*Figure 12. **A.** Fractional Exergy Distribution Available in feed streams. **B.** Relative Process & Thermodynamic Efficiency (Moreno et al., 2018).*

The Redstack pilot plant proved that the RED process efficiency increases at larger scales as shown in Figure 12 B), with negligible detriment to thermodynamic efficiency displayed in Figure 13 D). This also considers the greater pumping power demands required by the larger stacks displayed in Figure 13 C).
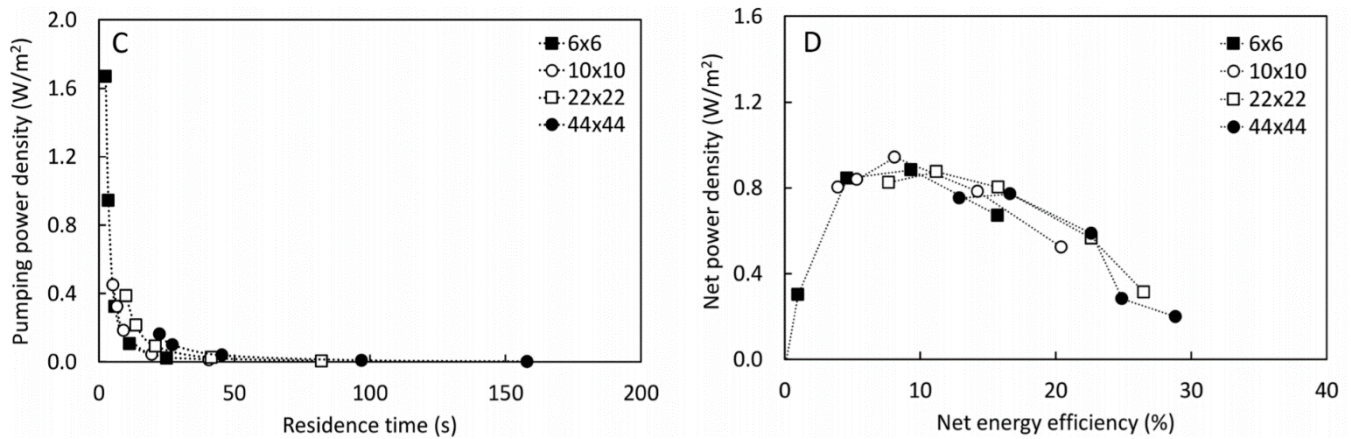
Figure 13. RED Performance Metrics (Moreno et al., 2018).

2.5.2 REAPower – Italy

Before development, the REAPower (Reverse Electrodialysis Alternative Power) team validated operational performance using process and fluid dynamic simulations specific to RED at higher ionic concentrations (Tedesco et al., 2015). Built on the salt works area in Marsala, Trapani, (west coast of Sicily) and financed by the European commission, the REAPower pilot plant uses brackish (0.034 – 0.051 M) water as the dilute solution and hypersaline (3.422 – 5.133 M) brine from saltworks for the concentrate (Ortiz-Imedio et al., 2019). It was the first plant globally to produce electricity from brackish and brine water. Figure 14 shows the layout of the plant, which utilises 2 stacks of 500 and 1 stack of 125 cell pairs (CP). All membranes were (44×44) cm^2, equating to roughly 400m^2 of total membrane area (Tedesco et al., 2017). For 5 months the stacks were tested with artificial solutions and achieved 2.6W/m^2. When real solutions were incorporated, a decrease in efficiency of up to 50% was seen. This was due to larger ions, such as Mg^{2+} being prevalent in the real feed solutions, of which caused a decrease in permeation efficiency and more frequent membrane fouling in comparison to the artificial ideal solutions (Tedesco et al., 2017). A fix for this issue could be the fractioned crystallisation process that would synergically enable the recovery of valuable Mg(OH)$_2$ from the brine effluent (Cipollina et al., 2012). Although the performance of the pilot plant reduced by half, it did not fall any further over extended periods of operation, implying continuous operation may be feasible (Tedesco et al., 2017).
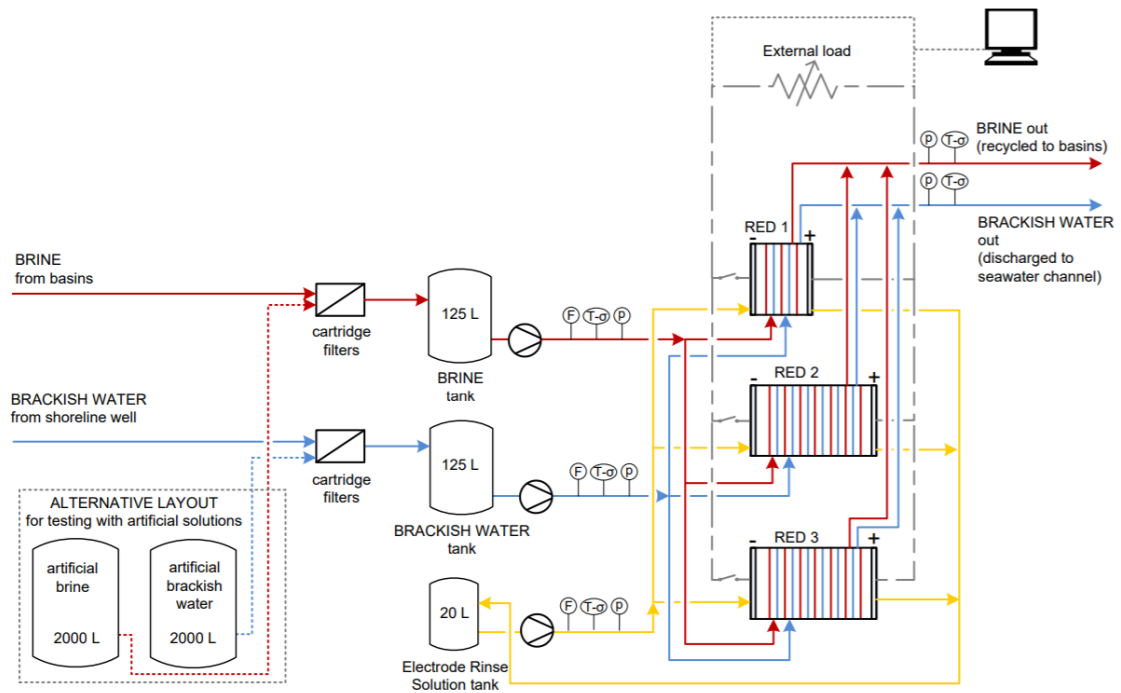
Figure 14. Process Flow Diagram of the REAPower Pilot Plant (Tedesco et al., 2017).

From the computational fluid dynamic modelling and simulations, the nominal power output of the pilot plant under ideal conditions was estimated to be 1kW. These models assumed that all 3 stacks had 500 cell pairs of (44×44) cm^2 membranes. In practice, only 2 such stacks were employed and the third was significantly smaller at only 125 CP, as shown in Figure 15. The pilot plant still achieved an output of 700W which was only 30% lower than what was predicted if using 3 full sized stacks under perfect conditions (Tedesco et al., 2017).
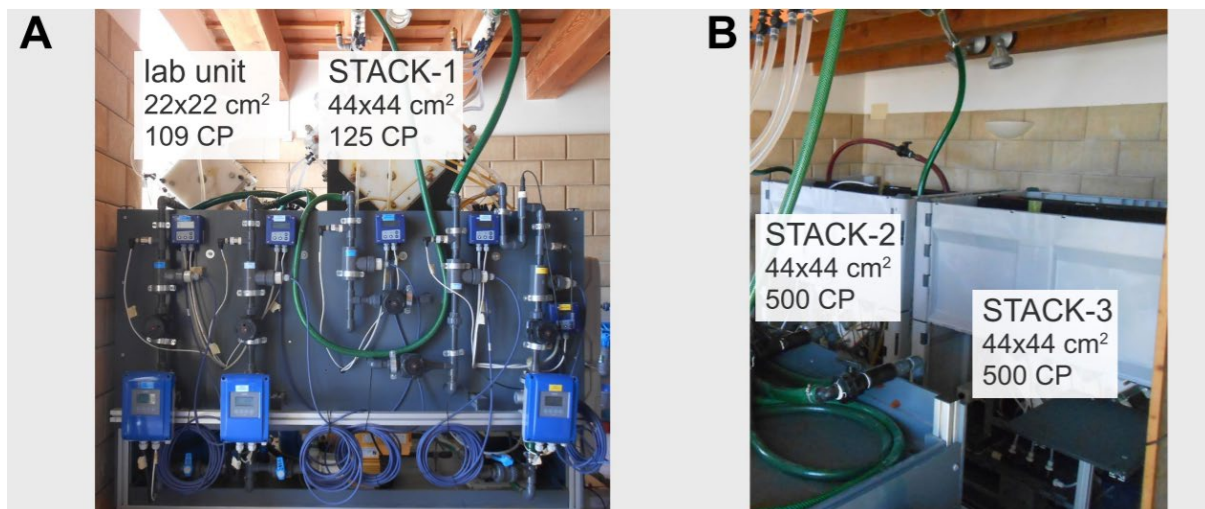
*Figure 15. **A.** First Stack, 375 CP Smaller Than What Was Employed in Computational Model. **B.** Second and Third Stacks (REAPower, 2014).*

The REAPower pilot plant not only validated the use of highly saline feed streams for RED but also the scalability of the process. 330W of gross power was generated using real feed solutions displayed in Figure 16 B) and a maximum power density of 1.6 W/m^2 relative to real feed streams as shown in Figure 16 A) (Tedesco et al., 2017).
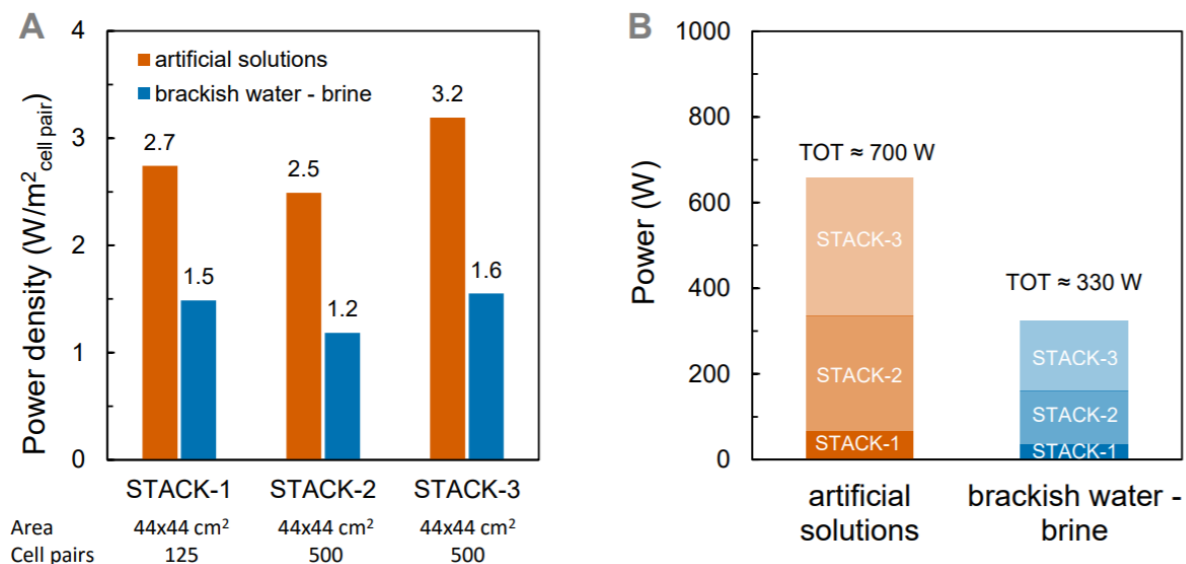
Figure 16. Performance Characteristics of REAPower Stacks. Real Brackish Solution (3.4 mS/cm) & Brine (190-215 mS/cm). Artificial Solutions (NaCl) of Same Conductivity (Tedesco et al., 2017).

2.6 RED WITH SWRO

There are currently no electrical energy reduction strategies associated with SWRO desalination as most of the processes energy reduction is derived from the recovery of hydraulic pressure in the effluent streams (Yoon et al., 2019). These ERDs are able to re-capture up to 95% of the pressurised hydraulic energy in the effluent back into the feed stream, greatly improving efficiency (Sanz et al., 2007; Voutchkov & Semiat, 2008). Other efforts have been in the optimisation of pre-treatment processes to limit membrane fouling/scaling as to minimise the rate of decrease in performance over the membrane life span (Elimelech & Phillip, 2011). The largest power consumption in a SWRO plant comes from the hydraulic pressure required to inverse the inherent osmotic pressure (reverse osmosis), forcing the permeation of potable water through the polyamide membranes (Ghaffour et al., 2013). Hybridisation of salinity gradient power technologies is an emerging theory in the efforts towards low energy SWRO (Achilli et al., 2014) as the two processes can operate symbiotically, depicted in Figure 17.
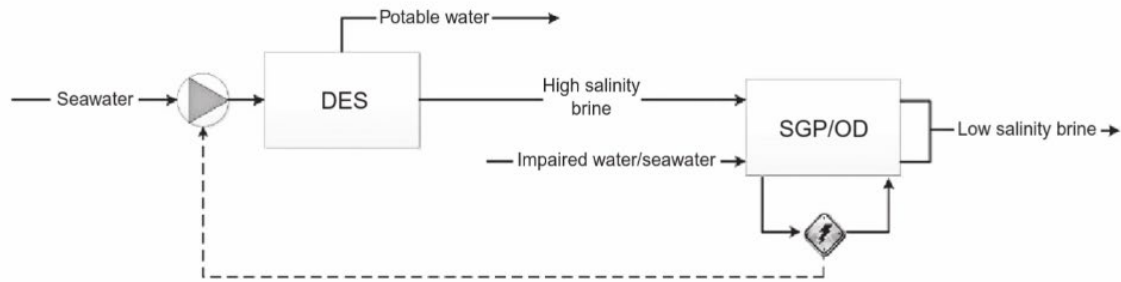
Figure 17. Symbiotic Pairing of Desalination (DES) and SGP Energy Recovery (Vanoppen et al., 2016). OD: Osmotic Dilution

The implementation of RED as a post treatment SWRO energy generation unit was rarely modelled due to the earlier, low perm-selective membrane characteristics, thus concluding the mixing of seawater with SWRO brine resulted in negligible power densities. Newer models using current knowledge and up to date membranes are estimating net energy densities of 4 W m^{-2} when utilising brine of 2M for the concentrate feed and 0.045M for the diluate as show in Figure 18.
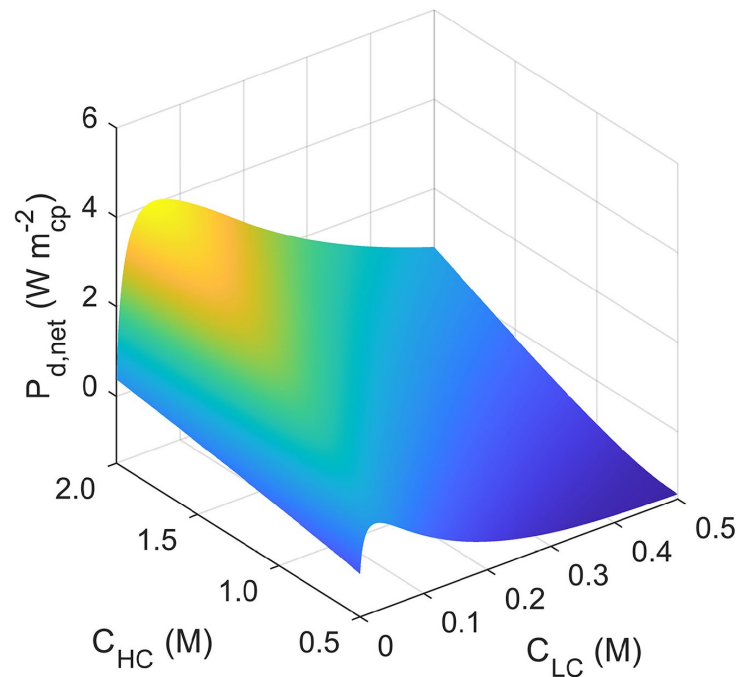
Figure 18. RED Model Utilising 2M SWRO Brine (Tristán et al., 2020).

2.7 RED + FO WITH SWRO

Forward osmosis (FO) refers to a dilution process that employs the salinity gradient between solutions and subsequent osmotic pressure to generate a driving force for water transport through a semipermeable membrane (Beaudry et al., 1999). These membranes separate a feed and draw (higher salinity compared to feed) solution. As the feed solution has a lower salinity than the draw solution,

an osmotic pressure is inherently generated, this 'draws' water from the feed solution separating the solutes from the feed stream and diluting the draw stream (Chung et al., 2012). As an example, sea water can be used as a draw solution and river water as a feed solution. Passing them alternately over a semipermeable membrane will result in a diluted seawater solution at the cost of fresh (river) water. This process generates a hydraulic head in the draw chamber as a volume of water passes from low to high concentration compartments. This volumetric flow of liquid can be utilised to spin a turbine and subsequently generate an electric current. Pilot plants such as Statkraft in Norway have been producing power in this way since 2009 (Skilhagen et al., 2008). In comparison to RO, FO has a larger rejection range of solutes/particulates and requires much less hydraulic pressure. The membranes utilised in FO have a lower propensity to fouling than RO which allows for a longer service life and less frequent maintenance regimes (Beaudry et al., 1999).

A hybrid combination of FO in conjunction with RED is of interest due to other low salinity feed solutions that otherwise get pumped into the sea as effluent, such as treated wastewater (TWW). By using a waste stream such as TWW for a feed solution it is possible to recover 'fresh' water that would otherwise be lost to the ocean. A benefit of having more diluted sea water is to subsequently run it through a SWRO plant. Instead of having pure seawater that requires greater hydraulic pressures to drive through SWRO membranes, a more dilute solution requires less energy to produce the same volume of drinking water. This does imply that a new set of membrane biofouling, pumping/plumbing, health/safety risk characteristics are introduced into the SWRO plant process as there's only a few membranes separating treated wastewater from the potable water that is to be distributed. A better method would be to simply generate power for the SWRO plant to offset the large energy requirements using a hybrid system of FO-RED as shown in Figure 19. By utilising a FO stage before RED, saltwater from the ocean is diluted with fresh water extracted from TWW that was destined for the sea. In doing so the salinity gradient is increased between the high and low concentration streams and results in a lower equilibrium concentration due to a diluted low concentration solution, which is a denominator term in the potential difference Eqn. (7) implying a greater capacity to generate power.
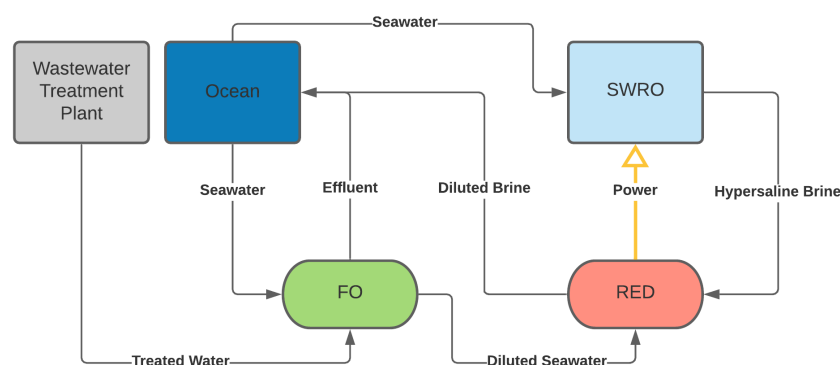
Figure 19. Hybrid FO-RED system for SWRO power generation using waste streams.

2.8 SUMMARY OF LITERATURE REVIEW

SGP offers a non-intermittent source of power that, until now, has only been available through the fossil fuel dependent power plants. This means that the system can be turned off or on to balance energy grid fluctuations with no detriment to efficiency. Compared to solar or wind of which are both more volatile than river or desalination flow rates. Current renewables also depend on the intensity of sunshine and air speeds respectively. RED simply requires the flow of globally abundant ionic solutions. There is a myriad of literature on critical parameters that determine the ultimate performance of the RED system such as the structure of membranes (Michele Tedesco et al., 2016), the geometry of spacers separating the membranes (Gurreri et al., 2016), influent solution concentrations (Tufa et al., 2014), flow rates through the stacks (Zhu et al., 2015) and stream temperatures (Brauns, 2009). Many constraints need to be overcome for RED to be competitive in the energy industry such as the scarcity of membranes made specifically for RED, the current high price and fouling characteristics of IEMs and the low practical power densities thereof (Zoungrana & Çakmakci, 2021). There are very few authors in the field analysing RED coupled with SWRO processes which makes establishing validity more challenging. There is an absence of parallel research into the optimisation of desalination technology and RED, possibly due to the scarcity of renewable energy research funding in the current fossil fuel based economic climate.

The most relevant parameter regarding a hybrid RED system relative to SWRO desalination is the effect feed concentrations have on system performance. If the dilute water stream is sourced from a river, roughly 45% of total ohmic losses are in the dilute passages due to the low conductivity (Veerman et al., 2009). This overall stack resistance can be minimised by using saline solutions in the dilute channels, such as diluted ocean water in conjunction with hypersaline brine, such as RO effluent in the concentrated channels to optimise conductivity and therefore performance (Tamburini et al., 2016).

In relation to feed stream parameters, assuming a constant/steady high concentration compartment (HC), increasing the salinity of the low concentration compartment (LC) yields conflicting results. The increase of free ions in solution results in higher conductivity/lower internal resistance, promoting power generation. However, it also reduces the difference in salinity between the HC and LC, reducing the electromotive force and subsequently the amount of power generation possible. In regard to flow rates, reducing residence time (increasing flow rate) within the stack increases the rate of ion migration and subsequently leads to higher electrical potential, this is at the cost of greater pumping requirements due to a larger pressure drop (Hong et al., 2013). In regard to feed stream temperature, greater gross power is achieved but lower perm-selectivity identified in the membranes. Higher temperatures have a beneficial influence on feed stream conductivity, diffusivity and membrane resistances, implying the higher the temperature, the greater the power generation capacity

(Ortiz-Imedio et al., 2019). The most interesting correlation found in literature is that utilising the greatest difference in salinity will not yield the maximum power output, although it is well established that power output will be maximised at LC concentrations below 0.1M. A balance between LC compartment conductivity, and subsequent ohmic resistance, needs to be achieved to optimise the process. If conditions can be identified in which a RED system can symbiotically generate meaningful power when coupled to a SWRO plant, RED could be a viable method of renewable energy generation to aid in low energy desalination.

3.0 MODEL DEVELOPMENT

Engineering Equation Solver (EES) is used in relation to the equations that match most accurately to the system performance parameters. The following model relies on the discretisation of the cell length (L) which is determined autonomously by the EES software. The following assumptions are also made:

- Co-current flow between compartments.
- HC and LC feed streams are purely sodium chloride solutions, hence not accounting for multivalent ions that are detrimental to RED efficiency (Gómez-Coma et al., 2019).
- Values are determined at average system conditions (feed stream concentration).
- The perm-selectivity of the membranes stay constant throughout the process, even though in practice they will vary with feed solution concentration and temperature (Ortega-Delgado et al., 2019; Zlotorowicz et al., 2017).
- The resistance of the membranes is independent to feed stream concentrations, even though the two are highly related at lower concentrations ($\sim 10^{-3}$ M) (Gómez-Coma et al., 2019; Kamcev et al., 2018; Park et al., 2006). This has been mitigated due to the relatively high concentrations utilised within this model and the fact that ohmic resistance outweighs that of the IEM at low concentrations in any case.
- Diffusivity coefficients of NaCl and water remain the same regardless of concentration and temperature.
- Each cell pair performs identically, thus assuming no ionic short circuiting and/or water leakage between the inlet manifolds. In practice, shunt currents in large scale RED stacks may have a prominent effect on the system's performance (Culcasi et al., 2020).
- Temperature effects the ohmic resistance of both AEM and CEMs identically.
- The pump(s) have a constant mechanical efficiency of 75%.

Although beneficial, cell pair modifications such as using conductive spacers instead of 'uncharged' plastic ones, yielding a threefold increase in power density (Długołęcki et al., 2010), or employing

wider HC compared to LC compartments (8:1), in which an 85% increase in power output was achieved (Hong et al., 2013), will not be included in the model due to the current lack of mathematical correlations for such conditions.

3.1 ELECTROKINETICS

In this model, a cell pair (CP) is defined as an AEM sandwiched between two CEM's. The voltage that is generated when co-current solutions of HC and LC are run alternately with the AEM separating them is evaluated by the Nernst equation (Hong et al., 2013; Tedesco et al., 2015).

$$E_{cell}(x) = \alpha_{CEM} \cdot \frac{R \cdot T}{F} \left[\frac{1}{z_{Na^+}} \ln \left(\frac{\gamma_{HC}^{Na^+}(x) \cdot C_{HC}^{Na^+}(x)}{\gamma_{LC}^{Na^+}(x) \cdot C_{LC}^{Na^+}(x)} \right) \right] + \alpha_{AEM} \frac{R \cdot T}{F} \cdot \left[\frac{1}{z_{Cl^-}} \ln \left(\frac{\gamma_{HC}^{Cl^-}(x) \cdot C_{HC}^{Cl^-}(x)}{\gamma_{LC}^{Cl^-}(x) \cdot C_{LC}^{Cl^-}(x)} \right) \right]$$

(11)

Where α_{CEM} & α_{AEM} are the perm-selectivity of the respective IEMS. F is Faraday's constant (96485.332 C/mol). C represents the ion concentration (mol/m^3) and z is the valence charge.

There is a myriad of activity coefficient models that have been developed for low molarity solutions, as depicted in Table 3.

Model	Equation	Valid Range
Debye-Hückel	$\log \gamma_i = -A z_i^2 \sqrt{I}$	I < 10$^{-2.3}$ M
Extended Debye-Hückel	$\log \gamma_i = -A z_i^2 \left(\frac{\sqrt{I}}{1 + B a_i \sqrt{I}} \right)$	I < 0.1 M
Davies	$\log \gamma_i = -A z_i^2 \left(\frac{\sqrt{I}}{1 + \sqrt{I}} - 0.3 \cdot I \right)$	I ≤ 0.5 M
Truesdell-Jones	$\log \gamma_i = -A z_i^2 \left(\frac{\sqrt{I}}{1 + B a_i^0 \sqrt{I}} \right) + b_i \cdot I$	I < 1 M
Pitzer	$\ln \gamma_\pm = -A_1 \left[\frac{\sqrt{I'}}{1 + b' \sqrt{I'}} + \frac{2}{b'} \ln(1 + b' \sqrt{I'}) \right] + m B^\gamma + m^2 C^\gamma$	I ≤ 6M

Table 3. Activity coefficient models and subsequent concentration validity range.

Only the Pitzer model of electrolyte thermodynamics can accurately describe ion-ion interactions at molarities exceeding 1M. As such, it is deemed an appropriate model for the case of the proposed RED systems (Pitzer, 1973). The virial equations were originally derived for the prediction of univalent electrolyte solutions under 6M and is accurate in doing so (Weber, 2000). It will therefore be employed to determine activity ($\gamma_\pm$) coefficients for the current model. I' represents the specific ion strength, m is the molality of the solution and A_1 is the modified Debye-Hückel coefficient (0.3215 at 298.15K). b' is a constant related to the valence ratio of the electrolyte (1.2 for valence electrolyte ratios of 1:1 such as NaCl). The virial coefficients *(B^γ, C^γ)* have been derived in Appendix A.

From Figure 20, which displays a synonymous electrical circuit diagram of a generic RED system, the electrical power generated (*E*) when an external load is connected (*R_L*) is quantified as the total theoretical voltage from the sum of voltages produced by the cell pairs within the stack while accounting for internal resistances (*R_{stack}*) (Mei & Tang, 2018).

$$E = \sum E_{cell} - j \cdot R_{stack}$$

(12)

Where E is measured in volts, $\sum E_{cell}$ represents the summation of CP voltages (V). *j* denotes electrical current density (A/m^2). R_{stack} is the summation of internal resistance within all the cell pairs (Ω·m^2). Hence, the generated voltage is the same as the voltage drop over the external load (*R_L*) measured in Ω·m^2. Figure 20 portrays the equivalent electrical illustration of a RED stack.

$$E = j \cdot R_L$$

(13)
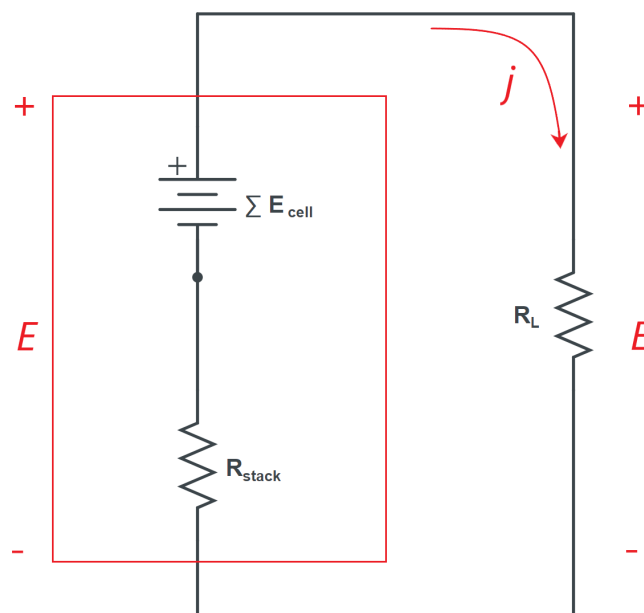
Figure 20. Synonymous circuit diagram of generic RED system.

Figure 21 shows the discretisation of the model in respect to the length of the cell (L = 0.383m) wherein the current density (I_d in this figure) changes in respect to its position in the system.
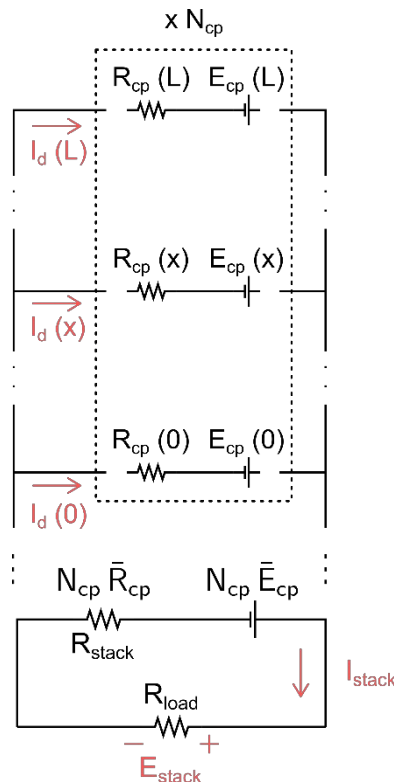
Figure 21. Equivalent Circuit Diagram Depicting Discretisation of L (Ortiz-Imedio et al., 2019).

Derived from Figure 21 and Eqns. (12) & (13), the current density (*j*) discretised along the compartment length is evaluated through Eqn. (14).

$$j(x) = \frac{\sum E_{cell}(x)}{R_{stack}(x) + R_L}$$

(14)

A second visual depiction of the current density (A m^{-2}) term is shown in Figure 22. This is a good representation of how the power generation capacity diminishes as the respective ions in the feed solutions permeate through the IEMs in a superficial linear direction (γ in this figure). This causes the ionic strength to decrease and increase in the high and low concentration compartments respectively. Thus, reducing the flux in respect to L and subsequently the salinity gradient between the streams. In this sense, the maximum current density is generated when the feed solutions first enter the stack (L=0), which implies the lower the residence time of the solutions in the stack, (the faster the streams move through the system) the greater the amount of energy generation is possible. This is mutually bound in an inverse relationship to the amount of pumping power required to move the solutions through the system, as the faster the linear velocity (lower residence time), the more pumping power

is required. Hence, implying there is an optimal balance between feed solution flow rates and power generation.
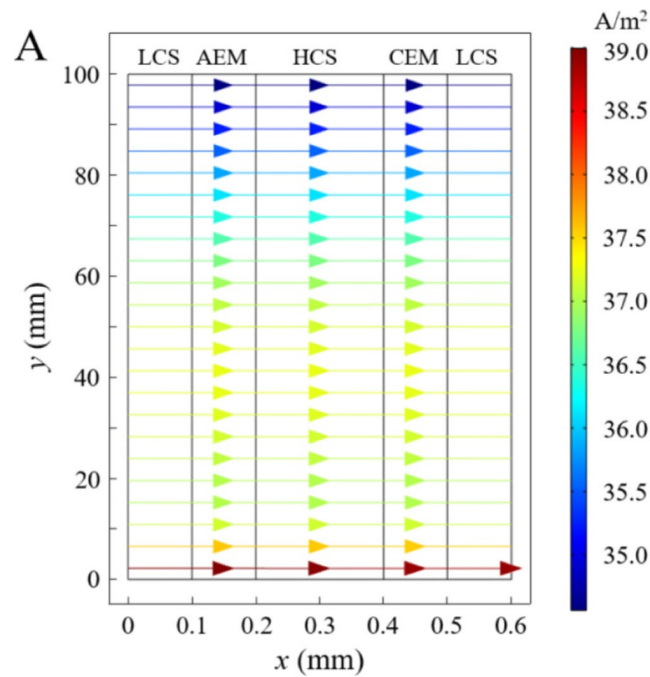
Figure 22. Current Density Changing in Respect to Membrane Length (Jin et al., 2021).

3.2 OHMIC RESISTANCES

The total internal resistance (R_i) within a RED stack is the sum of CP resistances in series (Hong et al., 2015). These resistances can be mostly split into ohmic/non-ohmic divisions as described by Eqn. (15). (Mei & Tang, 2018; Post et al., 2008). The internal resistance can also be determined through the experimental methods described in the works of Vermaas et al. (Vermaas et al., 2012; Vermaas et al., 2011a, 2011b).

$$R_i(x) = R_{ohmic}(x) + R_{non-ohmic}(x)$$

(15)

R_{ohmic} is generated by charge resistivity within the membranes themselves and the resistance experienced by the HC and LC solutions within their respective compartments measured in $\Omega \cdot m^2$ (Hong et al., 2013; Post et al., 2008; Vermaas et al., 2012). This is described by Eqns. (16) & (17).

$$R_{ohmic}(x) = R_{AEM} + R_{CEM} + R_{HC} + R_{LC}$$

(16)

$$R_{ohmic}(x) = R_{AEM} + R_{CEM} + \frac{\varepsilon_L}{\varepsilon^2 \cdot EC_{HC}(x)} + \frac{\varepsilon_L}{\varepsilon^2 \cdot EC_{LC}(x)}$$

(17)

Wherein R_{AEM} and R_{CEM} are the membrane resistances in $\Omega \cdot m^2$, EC_{HC} & EC_{LC} is the specific conductance in the HC and LC solutions respectively in Siemens (S/m). ε_L is the height of the spacer (m) and ε is the porosity of the spacer (-).

Temperature also has an effect on the ohmic areal resistance of the IEMs as proven by (Mehdizadeh et al., 2019). In which the empirical equation is:

$$R_{IEM}(T) = \frac{R_{IEM(0)}}{1 + 0.027(T - T_{ref})}$$

(18)

The authors described temperature affecting both AEM and CEMs nearly identically and as such will share the same equation, wherein $R_{IEM(0)}$ is the specified resistance from the manufacturer and T_{ref} is 298.15 K.

Electrical conductivity (EC) or specific conductance is an imperative water quality parameter regarding RED applications. It is easy to measure experimentally using a calibrated conductivity meter/probe. However, it is not so trivial to model mathematically. EC denotes the ease of electron migration through solution and subsequently affects the performance of the stack directly. EC of an electrolyte is a function of temperature and concentration, or in other words, dependent on the amount of ions existent in the solution. Hence, EC denotes the concentration of dissolved major ions in solution, of which enables the liquid to conduct an electric current through ion migration and/or changes in ion valence states within the ERS. It is defined as the reciprocal of the resistivity within the fluid normalised to $1cm^3$ at standard temperature and pressure. The unit for EC is S/m (Miller et al., 1988).

Molar conductivity (Λ_m), as described by equation (19), refers to the conductivity of an electrolytic aqueous solution at a concentration of 1 mol/L when placed between a cathode and an anode that hold a potential difference at a displacement of 1cm. The units for molar conductivity are $(S \cdot cm^2)/mol$. Where C refers to the molarity of solution in mol/L.

$$\Lambda_m = \frac{EC}{C}$$

(19)

Equivalent conductivity is defined as the normality of the solution, as opposed to molarity. This details the fact that ions with a greater valence (z) can carry a larger charge. Hence, the equivalent concentration is described by equation (20).

$$C_{eq} = \frac{|z|}{C}$$

(20)

Thus, equivalent conductance is described by equation (21).

$$\Lambda_{eq} = \frac{EC}{C_{eq}}$$

(21)

Regarding strong electrolytes, the molar conductivity will reach an effective limit as the solution becomes increasingly diluted (C → 0). This is called the limiting molar conductivity or molar conductivity at infinite dilution (non-interacting ions) and is represented by Λ_m^0. So $\Lambda = \Lambda^0$ when C = 0. Between 1875-1879, a German physicist by the name of Friedrich W.G. Kohlrausch determined that strong electrolytes at infinite dilution (completely dissociated), have each of their cations and anions provide a specific contribution to the equivalent conductance of an electrolytic solution. Known as Kohlrausch's law of the independent migration of ions.

$$\Lambda_m^0 = v_+ \Lambda_m^+ + v_- \Lambda_m^-$$

(22)

In which v_+ and v_- are the stoichiometric coefficients. Values for limiting molar conductivities can be found in literature and are regarded as constants at standard temperature and pressure. The following examples represent molar conductivities and diffusion coefficients for both individual cations and anions at 25°C.

Cation	Λ_m^+	$D_i / 10^{-9}$	Anion	Λ_m^-	$D_i / 10^{-9}$
	[S cm^2 mol^{-1}]	[m^2/s]		[S cm^2 mol^{-1}]	[m^2/s]
H$^+$	349.60	9.31	OH$^-$	197.67	5.27
Na$^+$	50.10	1.33	Cl$^-$	74.35	2.03
K$^+$	73.60	1.96	Br$^-$	75.50	2.01

Table 4. Ionic conductivity and diffusion at infinite dilution (Vanýsek, 1992)

In general, the *molar* conductance of an electrolyte will increase with dilution, as in the lower the molarity of the electrolyte, the more conductive it will become *per mol*. However, the specific conductance (EC) will decrease as ion-ion interaction lessens in frequency. Thus, we introduce Kohlrausch's law for strong electrolytes "The Square Root Rule". This law provides a correlation between molar conductivity and concentration, but it is only applicable to strong electrolytes at low concentrations (C ≤ 10mM) (McCleskey et al., 2012).

$$\Lambda_{eq} = \Lambda_{eq}^0 - K\sqrt{C_{eq}}$$

(23)

Which equates to

$$\Lambda_m = \Lambda_m^0 - K'\sqrt{C}$$

(24)

Where K is a known as the Kohlrausch's coefficient and K' is $K/|z|^{1.5}$. This parameter depends on the type of solvent and solute employed. It is determined through fitting the molar conductivity (Λ_m) vs.

the square root of molarity ($C^{0.5}$). In this sense the limiting molar conductivity (Λ_m^0) is the y-intercept for the linear regression and *K* is a negative gradient. Given experimental data, the Kohlrausch's coefficient can be determined from experimental molar conductance of NaCl, displayed in Table 5, and as seen in Figure 23. Thus, suggesting K = -0.0055. Note that Λ_m^0 of NaCl is the cumulative sum of the molar conductivities from the constituent ions at infinite dilution (refer to Table 4), which can be seen as the y-intercept in Figure 23: [124 S cm^2 mol^{-1}].

Concentration (mol·L^{-1})	Molar Conductance (S·m^2·mol^{-1})
0.1	10.674
0.01	11.851
0.0001	12.374

Table 5. Experimental Findings for the molar conductance of NaCl (Yadav, 2013)
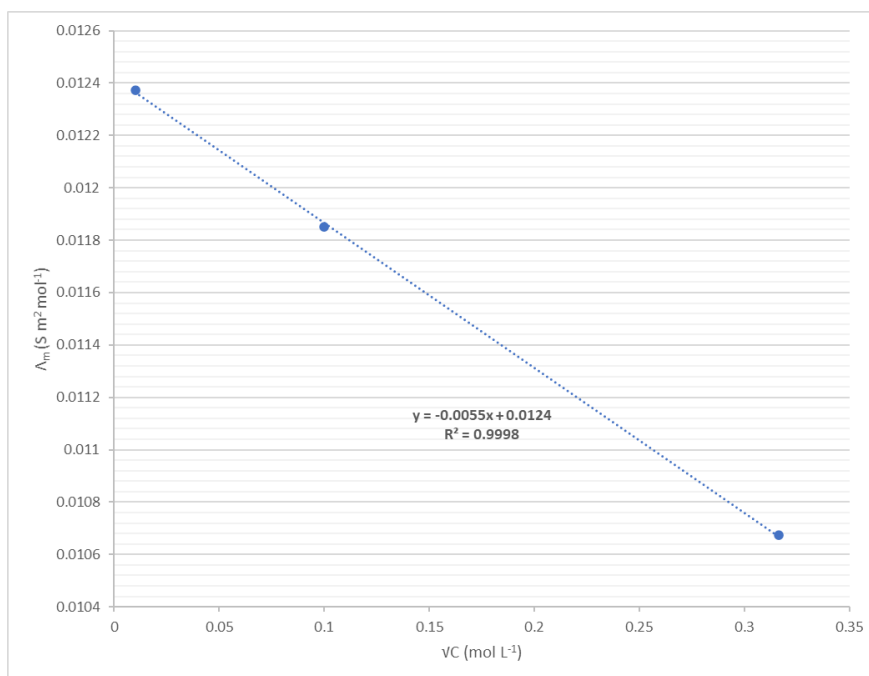
Figure 23. Determination of the Kohlrausch's coefficient based on experimental data (Yadav, 2013).

In this way, we end up with an EC equation for ideal solutions in which infinite dilution is applied (C approaches zero) summated across all dissolved ions *i* (solutes) multiplied by the concentration. $\Lambda_{m,i}$ is the contribution of the represented ion to the specific conductance. This is the Nernst-Einstein equation; however, it is accurate for limiting molar conductivities only.

$$EC^{(0)} = \sum_i \Lambda_{m,i}^0 \, c_i = \sum_i \Lambda_{eq,i}^0 \, |z_i| c_i = \left(\frac{F^2}{RT}\right) \sum_i D_i z_i^2 c_i \tag{25}$$

Where D_i is the respective diffusion coefficient. Real solutions are dependent on molar conductivities, hence deriving the equation for the non-ideal scenario:

$$EC = \sum_i \Lambda_{m,i} \; c_i = \sum_i \Lambda_{eq,i} \; |z_i| c_i$$

(26)

proposed by (Appelo, 2017) in which all ion-ion interactions are described by a corrected activity factor.

$$EC = \sum_i \Lambda^0_{m,i} \; \gamma_{corr} c_i$$

(27)

With

$$\gamma_{corr} \cong exp \left[-\frac{K}{\Lambda^0_{m,i}} \; |z_i|^{1.5} \; \sqrt{I} \; \right]$$

(28)

Where I (or μ) is the ionic strength of the solution as described by equation (29).

$$I = \frac{1}{2} \sum_i z_i^2 c_i$$

(29)

Hence

$$EC = \sum_i \Lambda^0_{m,i} \; (\gamma_i)^\alpha c_i$$

(30)

Where γ_i is the ion specific activity coefficient and α can be determined through:

$$\alpha = \frac{\ln \gamma_{corr}}{\ln \gamma_i} = \frac{K}{\Lambda^0_{m,i} \; (\ln 10) \; A \; |z_i|^{0.5}}$$

(31)

Wherein A is equal to 0.5085 M$^{-0.5}$. It can be noted that K is a non-trivial coefficient that can only be derived through experimentation. It is also sparsely available in literature so, again, proposed by (Appelo, 2017) is a parameterisation of the correction factor in which we negate it entirely:

$$\alpha = \begin{cases} 0.6/|z_i| & if \; I \; \leq 0.36 \; |z_i| \\ \sqrt{I}/|z_i| & otherwise \end{cases}$$

(32)

Hence, at 25C:

$$EC_{25}(x) = \left(\frac{F^2}{RT} \right) \sum_i D_i z_i^2 (\gamma_i)^\alpha c_i$$

(33)

Temperature also has an effect on the conductivity of an electrolyte. A rise in temperature boosts electrolytic conductivity through two primary methods. The first being ionic mobility. As temperature increases, the attraction between ions in solution is reduced, hence reducing the resistance of those ions to migrate through the solvent (lower bulk liquid viscosity). This suggests they don't tend to group together as frequently and are more homogenously distributed. Thus, permitting ease in electron transference as the rate of specific ionic interactions is amplified (Hwang et al., 2017). The

second is the degree to which the electrolyte dissociates, of which increases in respect to higher temperatures. This denotes the fraction of the solute that remains in ionic form (dissociated) within the solution as opposed to the non-dissociated ionogenic form. Permitting a greater number of free ions to be available in solution for conduction (Benneker et al., 2018). Herein, it can be seen that there is a fundamental correlation between electrical conductivity (EC), fluid viscosity, temperature and subsequent diffusion coefficients. A linearisation of this correlation is used regularly in which conductivity increase 2% for every degree increase (Hayashi, 2004). This is fairly robust but deviates substantially at higher temperatures as seen in Figure 24. The linearisation will subsequently not be incorporated into the model.
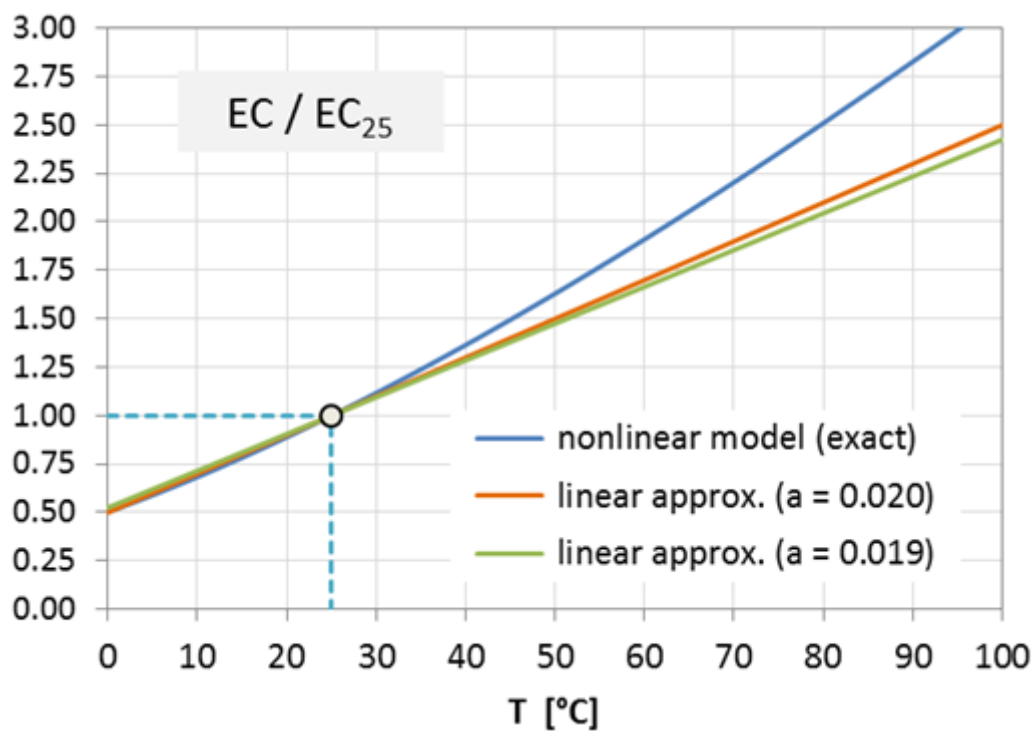
Figure 24. Comparison of linearisation and non-linearisation of EC model with temperature (aqion, 2021).

The Nernst-Einstein equation denotes the directly proportional interrelationship between EC and the respective diffusion coefficients as seen in Table 5.

$$EC = \left(\frac{F^2}{RT}\right) D_i z_i^2 c_i = const \cdot \frac{D_i}{T}$$

(34)

The Stokes-Einstein equation states the proportionality between the dynamic viscosity of the solution and the diffusion coefficients, described by:

$$D_i = \frac{k_B T}{6\pi \cdot \eta \cdot r}$$

(35)

In which k_B is the Boltzmann constant and r refers to the hydraulic radius of the dissociating ion. r can be ignored when focusing on η and D at varying temperatures, T_1 and T_2 for example, as it cancels out:

$$\frac{D_1/T_1}{D_2/T_2} = \frac{\eta_2}{\eta_1}$$

(36)

Equation (34) proves that there is a direct proportionality between EC and D/T, yielding:

$$\frac{EC_1}{EC_2} = \frac{D_1/T_1}{D_2/T_2} = \frac{\eta_2}{\eta_1}$$

(37)

Therefore, the temperature correlation with EC becomes the rearrangement of Eqn. (37):

$$\frac{EC}{EC_{25}} = \frac{\eta_{25}}{\eta}$$

(38)

Herein, demonstrating the compensation of EC with temperature in respect to EC and viscosity at 25°C. The dynamic viscosity of H_2O lessens with rising temperature as shown in Table 6.

Temperature (°C)	Dynamic Viscosity η (kg·m^{-1}·s^{-1})
20	$1.003 \cdot 10^{-3}$
25	$0.891 \cdot 10^{-3}$

Table 6. Change in dynamic viscosity of pure water with temperature (Atkins & De Paula, 2011).

A parameterisation of dynamic viscosity of pure water is proposed in the classical Atkins book of physical chemistry (Atkins & De Paula, 2011) in which a non-linear description of viscosity over the entire liquid range is derived with under 1% deviation to experimental findings.

$$Log\left(\frac{\eta_{20}}{\eta}\right) = \frac{A}{B} \quad or \quad \left(\frac{\eta_{20}}{\eta}\right) = 10^{A/B}$$

(39)

Where A and B are functions of temperature described in Appendix A. Therefore, by substituting Eqn. (39) into (38), we derive:

$$\frac{EC}{EC_{25}} = \left(\frac{\eta_{25}}{\eta_{20}}\right)\left(\frac{\eta_{20}}{\eta}\right) = \left(\frac{\eta_{25}}{\eta_{20}}\right)10^{A/B}$$

(40)

An arbitrary constant can be calculated from the terms in Table 6 ($\eta_{25}/\eta_{20} = 0.889$). Allowing the final derivation of a temperature dependent specific conductivity equation in the form of:

$$EC(x) = 0.889 \cdot 10^{A/B} \cdot EC_{25}$$

(41)

As concentration changes in relation to the discretised fluid's position (x) in the system, conductivity also changes in respect to L.

3.3 NON-OHMIC RESISTANCES

$R_{non-ohmic}$ is divided between R_{BL} and $R_{\Delta C}$. Wherein R_{BL} is the resistance due to concentration polarisation, which is a phenomenon where a gradient in ionic concentration occurs over the IEM, depicted in Figure 25 & Figure 26. The polarisation effect causes a difference in ion mobility or a 'bottleneck' in the transport of ions. The topographic plot of Figure 25 again uses γ to describe the length of the membrane (L) but is very useful in visually representing the valleys in concentration that occur at the solution/membrane interfaces, otherwise known as the boundary layer.
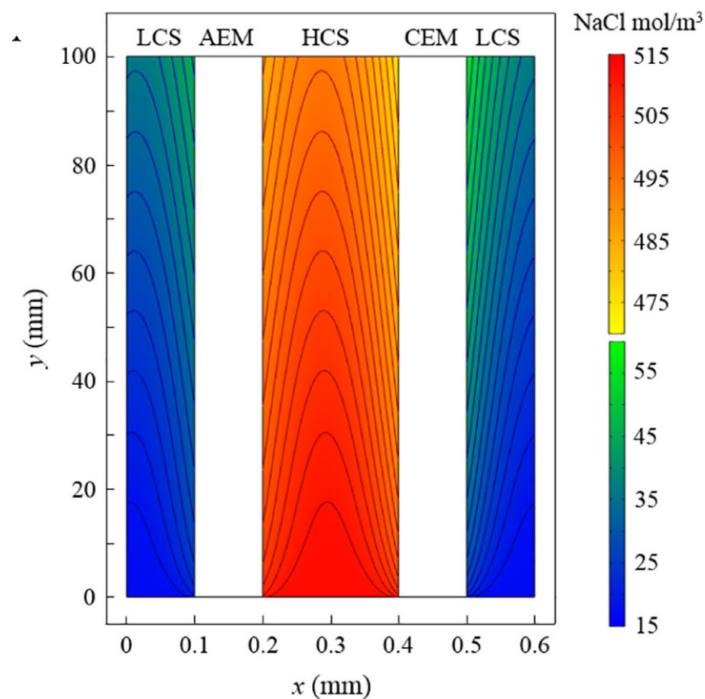
Figure 25. Depiction of Concentration Polarisation Phenomenon in Respect to Membrane Length (γ) (Jin et al., 2021).

This phenomenon causes a lower flux in the IEM due to the concentration gradient facilitating diffusion on the LC interface and an intensification of ion prevalence in the HC, subsequently generating a greater flux in the surrounding solutions, reducing specie permeation efficiency (Długołęcki et al., 2010).
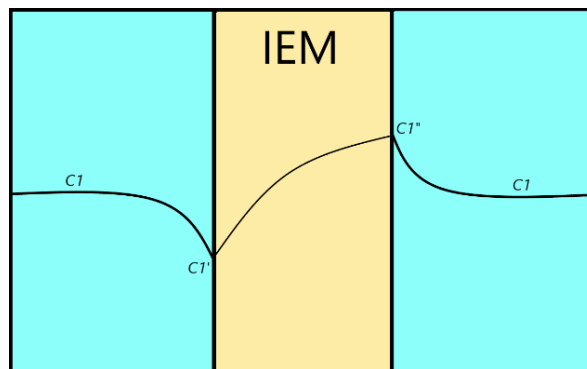
Figure 26. Concentration side profile over a cationic IEM and neighbouring solutions.

This concentration polarisation causes an inherent resistance to the boundary layer (R_{BL}) measured in $\Omega \cdot m^2$ (Zhu et al., 2015). This resistance is present over each IEM and is calculated through the equation described by (Vermaas et al., 2012):

$$R_{BL}(x) = 10^{-3} \cdot \left(0.62 \cdot \frac{tr(x) \cdot \varepsilon_L}{L} + 0.05 \right)$$

(42)

Wherein L represents the cell length (m), ε_L is the thickness (or height) of the spacer (m) & *tr* stands for residence time (s), defined by:

$$tr(x) = \frac{L \cdot b \cdot \delta \cdot \varepsilon}{Q(x)}$$

(43)

In which b is the width of the cell (m), ε is the porosity of the spacers (-) and Q is the volumetric flow rate per cell (m^3/s). The linear velocity of the solutions or the local superficial velocity (m s^{-1}) is described through:

$$v_{sol}(x) = \frac{Q(x)}{b \cdot \delta \cdot \varepsilon_L}$$

(44)

$R_{\Delta C}$ is the resistance caused from the change in concentration of the HC/LC solutions as they flow through their respective compartments between the inflow and effluent (Daniilidis et al., 2014; Hong et al., 2015; Vermaas et al., 2011a). Described by Eqn. (45).

$$R_{\Delta C}(x) = \frac{\alpha \cdot R \cdot T}{z \cdot F \cdot j(x)} \cdot \ln\left(\frac{\Delta_{LC}}{\Delta_{HC}}\right) = \frac{\alpha \cdot R \cdot T}{z \cdot F \cdot j(x)} \ln\left(\frac{1 + \frac{j(x) \cdot A}{F \cdot Q_{LC}(x) \cdot C_{LC}(x)}}{1 - \frac{j(x) \cdot A}{F \cdot Q_{LC}(x) \cdot C_{LC}(x)}}\right)$$

(45)

Where A is the surface area of a single membrane in m^2, Q is the volumetric flow rate per compartment in m^3/s and α is the average perm-selectivity (-). For this model, CEM's will be the outer IEM's. Hence the valence, z, referred to in equation (45) is that of Na$^+$ as the sodium ions will be responsible for the redox couple in the ERS and subsequently the migration of ions at the cathode/anode.

3.4 FLUXES

As both sodium cations migrate through the CEMs and chloride anions move through the AEMs from the HC to LC solutions, the total flux generated is described by Eqns. (46) & (47):

$$J_{Na^+}(x) = \frac{j(x)}{F} + \frac{D_{NaCl}}{\delta_m}\left(C_{HC}^{Na^+}(x) - C_{LC}^{Na^+}(x)\right)$$

(46)

$$J_{Cl^-}(x) = \frac{j(x)}{F} + \frac{D_{NaCl}}{\delta_m}\left(C_{HC}^{Cl^-}(x) - C_{LC}^{Cl^-}(x)\right)$$

<div align="right">(47)</div>

Wherein D_{NACl} is the diffusivity of salt m²/s and δ_m is the thickness of the membranes in m. The osmotic flux generated by solutions of different salinities between the IEMs causes water molecules to migrate through them from low to high concentration (Hong et al., 2013; Tedesco et al., 2015). The flux is described by Eqn. (48).

$$J_{H_2O}(x) = \frac{2D_{H_2O}}{\delta_m}\left(\left(C_{HC}^{Na^+}(x) + C_{HC}^{Cl^-}(x)\right) - \left(C_{LC}^{Na^+}(x) + C_{LC}^{Cl^-}(x)\right)\right)$$

<div align="right">(48)</div>

Where J_{H_2O} is the osmotic flux in (mol/(m²·s)) and D_{H_2O} is the diffusivity of water in m²/s. The fluxes in both the ionic and water fractions of the HC and LC solutions cause the concentration of salt to change over the distance they are in contact with IEMs in their respective compartments. The differential equations that describe this change in respect to membrane length are:

$$\frac{dC_{HC}^{Na^+}(x)}{dx} = -\frac{b}{Q_{HC}(x)} \cdot J_{Na^+}(x) - C_{HC}^{Na^+}(x) \cdot \frac{b \cdot J_{H_2O}(x)}{Q_{HC}(x)} \cdot V_{H_2O}$$

<div align="right">(49)</div>

$$\frac{dC_{HC}^{Cl^-}(x)}{dx} = -\frac{b}{Q_{HC}(x)} \cdot J_{Cl^-}(x) - C_{HC}^{Cl^-}(x) \cdot \frac{b \cdot J_{H_2O}(x)}{Q_{HC}(x)} \cdot V_{H_2O}$$

<div align="right">(50)</div>

$$\frac{dC_{LC}^{Na^+}(x)}{dx} = \frac{b}{Q_{LC}(x)} \cdot J_{Na^+}(x) - C_{LC}^{Na^+}(x) \cdot \frac{b \cdot J_{H_2O}(x)}{Q_{LC}(x)} \cdot V_{H_2O}$$

<div align="right">(51)</div>

$$\frac{dC_{LC}^{Cl^-}(x)}{dx} = \frac{b}{Q_{LC}(x)} \cdot J_{Cl^-}(x) - C_{LC}^{Cl^-}(x) \cdot \frac{b \cdot J_{H_2O}(x)}{Q_{LC}(x)} \cdot V_{H_2O}$$

<div align="right">(52)</div>

In which V_{H_2O} is molar volume of water in m³/mol (Veerman et al., 2008). The IEM utilisation can be recognized in Eqns. (49) & (50) where it is shown that the ionic concentration reduces in the HC compartment due to the ions migrating to the LC while water is simultaneously infiltrating the HC from the LC solution due to osmotic pressure. This process is inverted in the LC compartment (Eqns. (51) & (52)). As well as altering the salinity in the solution, the water flux also changes the flow rates within both the HC and LC compartments. Generating a greater flow rate in the HC and reducing it in the LC (Veerman et al., 2008). Described by equations (53) & (54).

$$\frac{dQ_{HC}(x)}{dx} = b \cdot J_{H_2O}(x) \cdot V_{H_2O}$$

<div align="right">(53)</div>

$$\frac{dQ_{LC}(x)}{dx} = -b \cdot J_{H_2O}(x) \cdot V_{H_2O}$$

<div align="right">(54)</div>

3.5 HYDRAULICS

In order to describe the hydraulic characteristics within the respective compartments, the Reynolds number (*Re*) is employed for standardisation. *Re* is depicted in Eqn. (55) where the intermembrane distance is half the hydraulic diameter. The volume taken up by the spacer is accounted for as porosity (Vermaas et al., 2014).

$$Re(x) = \frac{v \cdot D_h \cdot \rho}{\mu} = \frac{2 \cdot Q(x) \cdot \rho}{\varepsilon \cdot b \cdot \mu}$$

(55)

Where v represents velocity in m/s, D_h indicates the hydraulic diameter in m. ρ is the density of the fluids in kg/m^3. μ represents the dynamic viscosities in (kg/(m·s)). Density of water in respect to temperature is based off of the ITS-90 Volumetric Standards Calibration Formulation (Jones & Harris, 1992). Wherein

$$\rho = (999.83952 + 16.945176t - 7.9870401 \cdot 10^{-3}t^2 - 46.170461 \cdot 10^{-6}t^3 + 105.56302 \\ \cdot 10^{-9}t^4 - 280.54253 \cdot 10^{-12}t^5)/(1 + 16.897850 \cdot 10^{-3}t)$$

(56)

Where ρ is in kg/m^3 and t is the temperature in °C. To describe the pressure drop in a fully developed laminar flow through an infinitely wide and perfectly uniform channel the Darcy-Weisbach equation is used. This can then be modified and constrained to represent the two solution compartments for a cell pair through the revision of the spacer dependent hydraulic diameter. In this way, it is possible to model the distributed pressure drops in both the HC and LC compartments (Pa) (Tristán et al., 2020):

$$\frac{dp_{sol}(x)}{dx} = - \frac{48 \, \mu_{sol}(x, p, T) Q_{sol}(x)}{D_h^2 \cdot b \cdot \varepsilon_L \cdot \varepsilon}$$

(57)

$$D_h = - \frac{4 \, \varepsilon}{\frac{2}{\varepsilon_L} + (1 - \varepsilon) \cdot \frac{8}{\varepsilon_L}}$$

(58)

Where μ_{sol} is the local dynamic viscosity of the solution (Pa s). The Jones-Dole model is employed to correct the viscosity of aqueous solutions with the introduction of electrolytes.

$$\mu_{sol} = \mu_w \left(1 + \sum_{ca} \Delta\mu_{ca} \right)$$

(59)

In which μ_w is the viscosity of water (valid for 273.16-646.15 K) using coefficients found in the DIPPR database as described by Eqn. (60) (Thomson, 1996). $\Delta\mu_{ca}$ is the contribution to viscosity responsible by constituent ions in solution (*ca:* Na$^+$, Cl$^-$) derived through the Jones-Dole equation (61).

$$\ln \mu_w = -45.9352 + \frac{3703.60}{T} + 5.86600 \ln T - 0.587900 \cdot 10^{-28} \cdot T^{10}$$

(60)

$$\Delta \mu_{ca} = A_{ca} \cdot \sqrt{C_{NaCl}} + B_{ca} \cdot C_{ca}$$

(61)

In which C_{ca} is the concentration of the respective electrolytic solution (mol m^{-3}). The Aspen Physical Property System's database for aqueous solutions retrieves the temperature related coefficients for Eqn. (61) as A_{ca} equating to 5.011 m^2 and 7.634 m^2 for Na$^+$ and Cl$^-$ respectively. B_{ca} equates to 86.3 m^3 mol^{-1} for Na$^+$ and -7 m^3 mol^{-1} for Cl$^-$ (Tristán et al., 2020). When feed stream concentration exceeds 0.1M, the Breslau-Miller equation (62) is utilised.

$$\Delta \mu_{ca} = 2.5 V_e \cdot C_{ca} + 10.5 V_e \cdot C_{ca}^2$$

(62)

$$V_e = \frac{B_{ca} - 0.002}{2.60}$$

(63)

Where the univalent ion specific electrolytic volume is denoted by V_e in (63). The average pressure drop in each respective compartment (Δp_{HC}, Δp_{LC}) is the summation of pressure drops in each discretisation in respect to L. The amount of energy (W) required to surmount the inherent hydraulic resistance within each compartment is described by Eqn. (3) and by assuming a constant mechanical efficiency for the pump(s) (0.75) resulting in Eqn. (64).

$$P_{pump} = \frac{Q_{HC} \cdot \Delta p_{HC} + Q_{LC} \cdot \Delta p_{LC}}{\eta_{pump}}$$

(64)

4.0 DISCUSSION

4.1 MODEL VALIDATION

Using input parameters related to Perth's Seawater Desalination Plant (PSDP) in Kwinana, wherein the brine is discharged to Cockburn Sound at a molarity of 1.1M (65g/L) as proposed by the Water Corporation to the Environmental Protection Authority (Authority, 2009). In conjunction with Fumatech GmbH$^®$ IEM specifications, presented in section 7.1 of Appendix B. The optimal low concentration for RED is identified to be 86 mM in which a net power density of 3.14 W m^{-2} cp is achieved as displayed in Figure 27. This aligns with the finding (Tristán et al., 2020) who modelled a

gross power density of 4 W m^{-2} when implementing a brine of 2M for the concentrate feed and 45mM for the diluate as show in Figure 18. The consensus within literature, as discussed in Summary of Literature Review, is that maximum power density is achieved when concentrate molarity is maximised and the diluate concentration remains below 0.1M, of which this model agrees with, implying validity. Under the model assumptions, the higher molarity available for the HC stream, the more energy can be generated. This is due to a greater ratio of ion-ion activity between the two feed streams which enhances the chemical potential driving force (Giacalone et al., 2018; Giacalone et al., 2019; Ortega-Delgado et al., 2019; Tufa et al., 2015). This is at the cost of greater pumping power requirements due to a more viscous solution, but the detriment is negligible. Hence, why 2M (Figure 18) produces a higher net power density than 1.1M (Figure 27).

4.2 EFFECT OF CONCENTRATION

Figure 27 displays the RED relationship between an LC with a range of 0-500 mol m^{-3} (0-0.5M) in conjunction with a HC range of 1000-1200 mol m^{-3} (1-1.2M) at 25°C and an initial feed stream flow rate of 12 m^3 h^{-1}, corresponding to a local superficial linear velocity of 2.7 cm s^{-1}, in both compartments. These parameters were chosen to represent seawater and membrane based desalination effluent streams respectively in a Western Australian context. As discussed in RED + FO with SWRO, utilising a dilution process to bring the seawater molarity down to the optimal concentration will ensure the maximum power output of the stack. At these conditions, each square meter of cell pair membrane area will theoretically produce 3.14 W of electrical power. The HC and LC variables not only determine the possible SGP that can be produced as per Eqn. (11), but also the electromotive force (e.m.f) and inherent internal resistances, both ohmic and non-ohmic within the stack.
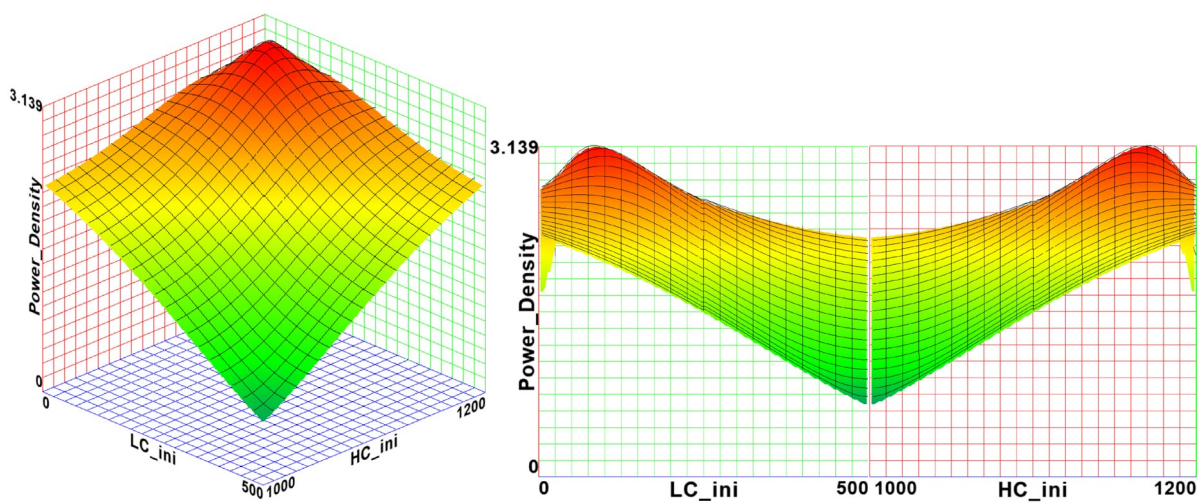

Figure 27. Effect of Concentration on RED Net Power Density.

Power Density: [W m^{-2} cp]

LC = HC: [mol m^{-3}]

HC_ini and LC_ini represent the initial (L=0) concentration of the concentrate and diluate feed streams respectively in mol m^{-3}. The discrepancy in optimal LC between this model and other studies (Ortiz-Imedio et al., 2019; Tedesco et al., 2015; Tristán et al., 2020; Veerman et al., 2011; Vermaas et al., 2012) is due to the fact that every specific HC concentration will have an individual and relative LC concentration in which power density is maximised, hence why optimal LC in Figure 27 is different to Figure 18 as the respective HC utilised is 1.2M & 2M. This crucial parameter will vary significantly from study to study due to the non-standardised methods in which the RED process is modelled in literature. Mainly in the determination of which equations and coefficients to employ for aspects such as ion activity and conductivity, of which heavily influence the system's performance at lower concentrations due to ohmic resistance in the LC and the shape of the activity curve utilised as shown in Figure 9. The model itself, and regularly entire equations and terms, are mitigated in literature. Most of the effort within this study was devoted to the reverse engineering of equations from the results backwards to determine the process which was followed to reach the subsequent result. Otherwise, equations had to be derived as was the case with conductivity.

Figure 27 infers an upward trend in power density as HC concentration increases. The dip in power density between HC: 1160-1200 mol m^{-3} is due to the parametric evaluation method that EES utilises. In this way, the lowest LC concentration is paired simultaneously with the greatest HC concentration. Such that the inherent ohmic resistance in the LC at very low concentrations negates the potential of high concentrate molarities. In actuality, a greater energy density can be achieved when employing higher concentrations. In this case, 1200 mol m^{-3} was inputted as a maximum HC molarity to offset the parametric effect of EES and optimise molarities that more closely resemble the brine effluent of PSDP (~1.1M).

The concentration of the LC compartment is the most influential parameter in the entire system. As the more dilute LC becomes, the less conductive it is. This is counterintuitive as the Nernst equation implies a greater capacity for power generation with a larger discrepancy between the feed solution concentrations. Which is true, however, this is undermined by the fact that the ohmic resistance increases as LC becomes less conductive (dilute), reducing the power output of the stack. Hence, a balance needs to be identified in which the counteractive parameters offer the greatest power density. The physical and thermodynamic properties of the feed streams are also influenced by their respective molarities. The energy required to pump the solutions through the stack increased by 7% when the HC concentration is increased from 0.3-1.2M due to a greater solution viscosity. Which results in marginally greater pressure drops within the compartments. However, this is negligible as the increase in gross power output due to higher HC molarities outweighs the necessary increase in pumping power.

4.3 EFFECT OF FLOW RATE

Power Density: [W m^{-2} cp]

$Q_{HC} = Q_{LC}$: [M^3 h^{-1}]
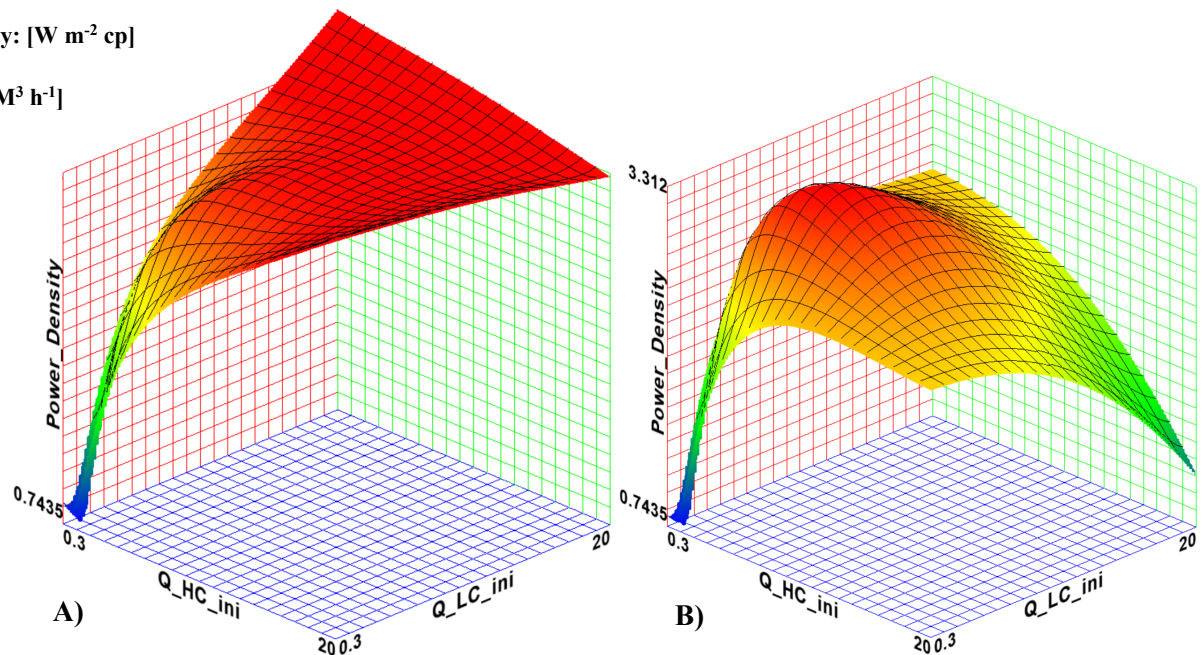
Figure 28. A) Gross B) Net Power Densities as a Function of Initial Feed Stream Flow Rates.

As optimal compartment concentrations are determined from Figure 27, the process can be optimised further by identifying the ideal flow rates of feed solutions through the RED system. The effect of feed stream flow rates through the system can be seen as gross and net power densities displayed in Figure 28. The electrolytic fluids at 25°C with initial flow rates in the range of 0.3-20 m^3 h^{-1}, at the pre-determined optimal concentrations are displayed in Figure 28. It is seen in A) that the faster the feed solutions move through the system, the greater the gross power density, rising steadily with increased volumetric flow. This is due to a rise in average current density, from a lower rate of ion permeation (greater concentration difference) across the membranes, and thus a greater chemical potential is maintained along the discretised length. Mathematically shown in Eqns. (49)-(52), inferring a greater capacity to generate energy until the concentration change in the feed stream approaches zero, at which increasing the flow rate further has negligible effect, displayed by the plateau region in the X-Y-Z plot. The gain in power density is also attributed to improved homogenous mixing of solutions, which not only minimises the non-ohmic resistances such as concentration polarisation and boundary layer concentration gradients, but also reduces the difference in exergy due to the two feed streams mixing more completely inside the stack. i.e. the ionic flux is increasingly converted into electromotive force (Moreno et al., 2018; Ortiz-Imedio et al., 2019). As increasing flow rate comes at the cost of pumping power due to larger hydrodynamic losses, Figure 28 B) shows that there is a point at which flow rate is optimised, namely, when the initial HC flow rate (Q_HC_ini) is equal to 4.49 m^3 h^{-1} and the initial LC flow rate (Q_LC_ini) is 6.51 m^3 h^{-1}. This implies

a High:Low compartment flow rate ratio of ~0.7 is optimal, subsequently increasing the net power density of the system to 3.31 W m^{-2} cp.

4.4 EFFECT OF TEMPERATURE

Power Density: [W m^{-2} cp]

LC = HC: [mol m^{-3}]
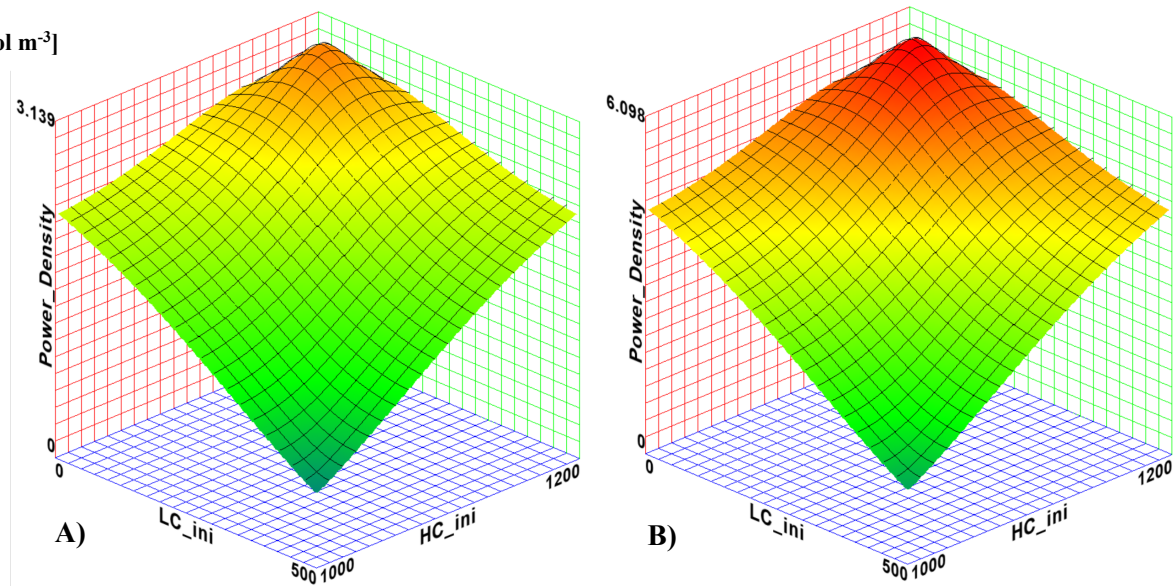
Figure 29. RED Power Density at A) 25°C, B) 55°C.

Although rarely influenced by the designer, as it is dependent on the location, the temperature of the feed streams entering the stack are very influential on the systems performance. Due to a combination of increased solution conductivity, decreased viscosity and lower membrane resistance (Eqn. (18)), the power density of the system increases linearly by ~0.1 W m^{-2} per K as shown in Figure 30. As feed solution viscosity changes with temperature, it is implied that new optimal flow rates should be determined at different influent stream temperatures in order to optimise the process at different operating conditions

The fact that hotter feed streams boost the power output of RED systems, infers that a substantial opportunity exists for desalination plants to not only increase the regeneration capacity through RED in hotter months when demand for fresh water peaks (Wa'el A et al., 2018) but also to utilise low grade industrial waste heat in the SWRO process. Machinery such as RO pumps can be retrofit with water-water radiator systems to transfer waste heat to the RED feed streams. Any increase in the electrolyte temperatures will be beneficial for not only power generation but also the efficiency of the pumps themselves.
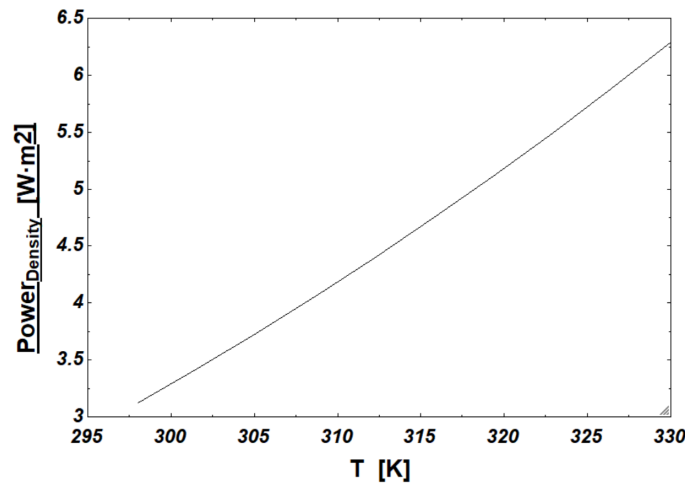
Figure 30. 0.099 W m⁻² Increase in Power Density per K.

4.5 SERIES-PARALLEL LAYOUT FOR MAXIMISING OUTPUT

As there is still a substantial amount of SGP available in the effluent after passing through a single stage of RED stacks (73%), it was proposed that a multi-stage series RED plant layout could offer the maximum power output from SWRO brine as each downstream stack would generate power from the unused SGP until the concentrations equalised to the point they were un-economical to harvest (Tristán et al., 2020).
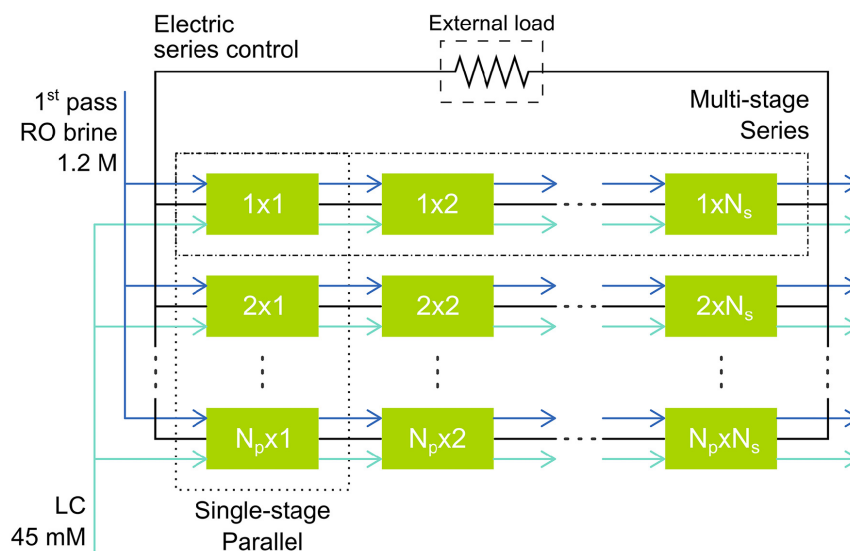
Figure 31. SGP-RED Plant Layout for Barcelona SWRO. N_p Parallel Units, N_s Stacks in Series (Tristán et al., 2020).

The maximum quantity of RED units that are viable for a parallel layout is derived through the division of the SWRO's brine effluent flow rate (180 ML day⁻¹) (Authority, 2009) by the optimal flow rate in the concentrated compartment at the design conditions (4.49 m³ h⁻¹). In this way, 1670 RED stacks composed of 1000 cell pairs with an effective membrane area equal to 0.175 m² per individual membrane would yield a net power output of 0.97 MW utilising an optimal power density of 3.31 W

m^{-2} cp in the first stage. As PSDP has an average power requirement 24.1 MW (4.2 kWh m^{-3}), a single stage of parallel RED stacks would recapture 4 % of the energy demand (Sanz et al., 2007). A multi-stage arrangement as shown in Figure 31 harvests the subsequent SGP that isn't captured from the previous stage, allowing for a greater fraction of SGP to be harnessed from the SWRO plant's brine. Utilising a further 4 stages (5 total), the net power output of the plant increases nearly threefold, increasing the capital expenditure (CAPEX) respectively. As each downstream stage has progressively less driving force, due to the feed stream concentrations approaching each other, the net power density reduces from 3.31 W m^{-2} cp in the first stage to 1.36 W m^{-2} cp in the fifth. This series-parallel arrangement provides a balance of energy yield, obtained in the series arrangement and power generation, obtained in the parallel network (Tristán et al., 2020). The maximum power output of this series-parallel layout yields 2.48 MW, or 10.3% of the plant's average energy demand through recovered salinity gradient power. Reducing the SEC required to produce 1m^3 of potable water at PSDP from 4.2 kWh to 3.8 kWh.

5.0 CONCLUSIONS / RECOMMENDATIONS

This study reveals the enormous potential for SGP to be recovered from the effluent streams of SWRO plants, however, it also reinforces the fact that there are still efforts to be made in not only the optimisation of RED process characteristics as to maximise net power output and efficiency but also in the minimisation of CAPEX and OPEX. Regarding the brine characteristics generated by PSDP, a 10.3% reduction in the SEC for a cubic metre of desalinated water is obtained when utilising seawater diluted with TWW (0.86M). Overall, a parametric evaluation of system parameters for a large scale SGP generation plant utilising RED is conducted to provide a multi-variable optimisation of the process. It is identified that hotter months lead to an increase in demand for desalinated water per capita, of which generates more brine, at higher temperatures. It is during this period that RED energy production is optimal. An economic analysis should be conducted to gain an understanding of the costs associated with the construction of such a power plant; however, it is not within the scope of this project. It is also recommended that the models themselves are included in subsequent studies. The effect of multivalent ions present in real solutions needs to be investigated further, to determine strategies that mitigate their detrimental nature. The energy efficiency and power density of the system are mutually bound in a conflicting relationship, further investigation is required to determine the optimal balance between the two for an industrial scale RED plant. This study proposes hybrid plant arrangements that may maximise net energy generation and minimise CAPEX and OPEX. The presented results have potential for subsequent integrated analyses that account for economic and technical constraints for the development of large scale, renewable, SGP generation plants utilising SWRO brine streams.

6.0 APPENDIX A.

6.1 DERIVATION OF PITZER COEFFICIENTS FOR VIRIAL EQUATIONS

The Pitzer virial equations have been opted for in the approximation of activity coefficients as they cover a wider range of electrolyte concentrations in comparison to other models mentioned.

$$B^{\gamma} = 2\beta^{(0)} + 2\beta^{(1)} \frac{\left[1 - \left(1 + \alpha m^{\frac{1}{2}} - \frac{\alpha^2 m}{2}\right) exp(-\alpha m^2)\right]}{\alpha^2 m} \tag{65}$$

$$B^{\varphi} = \beta^{(0)} + \beta^{(1)} e^{-\alpha}\sqrt{I} \tag{66}$$

$$C^{\gamma} = \frac{3}{2} C^{\varphi} \tag{67}$$

Where α is fixed ($(2 \text{ kg mol}^{-1})^{0.5}$). I is the ionic strength and m is the molality of the electrolytic solution. $\beta^{(0)}$ $\beta^{(1)}$ C^{φ} are functions based on the nature of the salt solution and must be determined through experimentation. The current model uses the findings of (Weber, 2000) in which.

$\beta^{(0)}$	$\beta^{(1)}$	C^{φ}
0.06743	0.3301	0.00263

Table 7. Binary interaction coefficients for NaCl in regards to Pitzer Virial equation determination (Weber, 2000)

6.2 NERNST-EINSTEIN / STOKES-EINSTEIN VISCOSITY RELATIONSHIP

$$A = 1.37023 \cdot (t - 20) + 8.364 \cdot 10^4 \cdot (t - 20)^2 \tag{68}$$

$$B = 109 + t \tag{69}$$

Where t is in °C.

7.0 APPENDIX B.

7.1 MODEL

At present and to the best of the author's knowledge, this will be the first time in literature the model itself is disclosed within the document. This aims to mitigate wasted time and energy in the progression of this technology.

Conductivity Function

Function **IfTest** (LC)

Appelo parametrisation for conductivity derivation - LC

$$\text{If } \left[\frac{LC}{1000} <= 0.36 \right] \text{ Then } \quad \alpha_3 := 0.6 \quad \text{Else} \quad \alpha_3 := \left[\frac{LC}{1000} \right]^{0.5} \quad \text{EndIf}$$

$$\text{IfTest} := \alpha_3$$

End **IfTest**

Environment Parameters

$T = 298.15$ Feed stream temperature [K]

$t_C = T - 273.17$ Temperature in [C]

$T_{crit} = 647.096$ Critical temperature in [C]

Physical Parameters

$Q_{HC,ini} = 0.001388$ Initial flow rate in the HC compartments [m^3/s]

$Q_{LC,ini} = 0.001388$ Initial flow rate in the LC compartments [m^3/s]

$dQ_{HCdx} = b \cdot J_{H2O} \cdot V_{H2O}$ Positive change to flow rate in HC

$dQ_{LCdx} = -b \cdot J_{H2O} \cdot V_{H2O}$ Negative change to flow rate in LC

$$Q_{HC} = Q_{HC,ini} + \int_{L_{in}}^{L_{end}} (dQ_{HCdx}) \, dx \quad \text{Dynamic rate of change to flow rate in HC in respect to L}$$

$$Q_{LC} = Q_{LC,ini} + \int_{L_{in}}^{L_{end}} (dQ_{LCdx}) \, dx \quad \text{Dynamic rate of change to flow rate in LC in respect to L}$$

$$tr_{HC} = \frac{L \cdot b \cdot \varepsilon_L \cdot \varepsilon}{Q_{HC}} \quad \text{Residence time in the HC compartment [s]}$$

$$tr_{LC} = \frac{L \cdot b \cdot \varepsilon_L \cdot \varepsilon}{Q_{LC}} \quad \text{Residence time in the LC compartment [s]}$$

$$v_{HC} = \frac{Q_{HC}}{\varepsilon \cdot b \cdot \varepsilon_L} \quad \text{local superficial linear velocity [m/s]}$$

$$v_{LC} = \frac{Q_{LC}}{\varepsilon \cdot b \cdot \varepsilon_L} \quad \text{Local superficial linear velocity [m/s]}$$

Electrical Parameters

$R_{load} = 1$ External load [ohm]

$E_{stack} = n \cdot E_{cell.avg} - I_{stack} \cdot R_{stack}$ Electric potential difference of the RED stack [V]

$$E_{cell} = \frac{R \cdot T}{F} \cdot \left[\alpha_{CEM} \cdot \frac{1}{z_{Na}} \cdot \ln\left(\frac{\gamma_{Na,HC} \cdot C_{Na,HC}}{\gamma_{Na,LC} \cdot C_{Na,LC}} \right) + \alpha_{AEM} \cdot \frac{1}{z_{Cl}} \cdot \ln\left(\frac{\gamma_{Cl,HC} \cdot C_{Cl,HC}}{\gamma_{Cl,LC} \cdot C_{Cl,LC}} \right) \right] \quad \text{OCV / Nernst potential of cell pair [V]}$$

$$I_{ext} = \frac{E_{stack,avg}}{R_{load}} \cdot b \cdot L \quad \text{Electric current through the external load [A]}$$

$$R_{stack} = n \cdot \frac{R_{cell,avg}}{b \cdot L} \quad \text{Internal resistance [ohm]}$$

$$I_{stack} = \frac{E_{stack}}{R_{stack} + R_{load}} \quad \text{Electric current flowing through the external load, generated by the stack [A]}$$

$$j = \frac{n \cdot E_{cell} - E_{stack}}{n \cdot R_{cell}} \quad \text{Electric current density in each parallel branch of the equivalent circuit, Fig 22. [A m}^{-2}\text{]}$$

Average cell pair resistance

$$R_{cell,avg} = \frac{\int_{L_{ini}}^{L_{end}} (R_{cell} \cdot x) \, dx}{\int_{L_{ini}}^{L_{end}} (x) \, dx + 1.0 \times 10^{-9}}$$

Average current density

$$j_{avg} = \frac{\int_{L_{ini}}^{L_{end}} (j \cdot x) \, dx}{\int_{L_{ini}}^{L_{end}} (x) \, dx + 1.0 \times 10^{-9}}$$

Average electric potential of a cell pair

$$E_{cell,avg} = \frac{\int_{L_{ini}}^{L_{end}} (E_{cell} \cdot x) \, dx}{\int_{L_{ini}}^{L_{end}} (x) \, dx + 1.0 \times 10^{-9}}$$

Average stack voltage

$$E_{stack,avg} = \frac{\int_{L_{ini}}^{L_{end}} (E_{stack} \cdot x) \, dx}{\int_{L_{ini}}^{L_{end}} (x) \, dx + 1.0 \times 10^{-9}}$$

$$P_{gross} = E_{stack} \cdot I_{stack} \quad \text{Gross power output of the stack [W]}$$

$$P_{net} = P_{gross} - P_{pump} \quad \text{Net Power output after pumping power requirements [W]}$$

$$Power_{Density} = \frac{P_{net}}{n \cdot b \cdot L} \quad \text{Power density [W m}^{-2}\text{ cp]}$$

Fluxes

$$J_{Na} = \frac{j}{F} + 2 \cdot \frac{D_{NaCl}}{\delta_{CEM}} \cdot (C_{Na,HC} - C_{Na,LC}) \quad \text{Sodium Flux (mol m}^{-2}\text{ s}^{-1}\text{)}$$

$$J_{Cl} = \frac{j}{F} + 2 \cdot \frac{D_{NaCl}}{\delta_{AEM}} \cdot (C_{Cl,HC} - C_{Cl,LC}) \quad \text{Chloride Flux (mol m}^{-2}\text{ s}^{-1}\text{)}$$

$$J_{H2O} = \frac{2 \cdot D_{H2O}}{\delta_{CEM}} \cdot (C_{Na,HC} + C_{Cl,HC} - (C_{Na,LC} + C_{Cl,LC})) \quad \text{Water Flux (mol m}^{-2}\text{ s}^{-1}\text{)}$$

$$V_{H2O} = \frac{M_{H2O}}{\rho_{water}} \quad \text{volumetric flux of water m}^{3}\text{ mol}^{-1}$$

Constants

$F = 96485.332 \quad$ Faraday's Constant [C mol^{-1}]

$R = 8.314 \quad$ Ideal Gas Constant [J K^{-1} mol^{-1}]

$D_{NaCl} = 4.56 \cdot 10^{-12} \quad$ Salt Permeability coeffieicent / Salt Diffusivity [m^2 s^{-1}]

$D_{H2O} = 1.01 \cdot 10^{-10} \quad$ Water Diffusivity [m^2 s^{-1}]

$M_{H2O} = 0.018015 \quad$ Molar mass of water [kg mol^{-1}]

Ion Specs

$z_{Na} = 1 \quad$ Valence charge, 1s22s22p63s1

$z_{Cl} = |-1| \quad$ Absolute Valence charge, 3s23p5

Membrane Specs

$A = L \cdot b \quad$ Surface area of a membrane [m^2]

$b = 0.456 \quad$ Width of a membrane, also known as cell width [m]

$L_{ini} = 0 \quad$ variable starting point

$L_{end} = L \quad$ variable end point [x]

$L = 0.383 \quad$ Length of a membrane, also known as cell length. This is what the model is discretised against [m]

$n = 1000 \quad$ Cell pairs

$\alpha = \frac{\alpha_{AEM} + \alpha_{CEM}}{2} \quad$ average membrane permselectivity

Spacer Specs

$\varepsilon = 0.825 \quad$ Porosity of spacer between membranes [%]

$\varepsilon_L = 0.00027 \quad$ Spacer thickness/height, 270 micro m, intermembrane distance [m]

Anion Exchange Membrane: AEM

$\delta_{AEM} = 0.00005 \quad$ [m] Thickness of membrane [m]

$\alpha_{AEM} = 0.94 \quad$ Permselectivity [%]

$$R_{AEM} = \frac{0.000105}{1 + 0.027 \cdot (t_C - 25)}$$ Temperature dependent areal resistance AEM [ohm m^2]

Cation Exchange Membrane: CEM

$\delta_{CEM} = 0.00005$ Thickness of membrane [m]

$\alpha_{CEM} = 0.98$ Permselectivity [%]

$$R_{CEM} = \frac{0.000215}{1 + 0.027 \cdot (t_C - 25)}$$ Temperature dependent areal resistance CEM [ohm m^2]

Concentrations

$HC_{ini} = 1000$ Initial concentration in HC compartment [mol m^{-3}]

$LC_{ini} = 10$ Initial concentration in LC compartment [mol m^{-3}]

$C_{Na,HC,ini} = HC_{ini}$ Initial concentration of Na ions in HC [mol m^{-3}]

$C_{Cl,HC,ini} = HC_{ini}$ Initial concentration of Cl ions in HC [mol m^{-3}]

$C_{Na,LC,ini} = LC_{ini}$ Initial concentration of Na ions in LC [mol m^{-3}]

$C_{Cl,LC,ini} = LC_{ini}$ Initial concentration of Cl ions in LC [mol m^{-3}]

$$dC_{Na,HCdx} = -\frac{b}{Q_{HC}} \cdot J_{Na} - C_{Na,HC} \cdot \frac{b \cdot J_{H2O}}{Q_{HC}} \cdot V_{H2O}$$ Na ions permeate from HC to LC, negative change to HC

$$dC_{Cl,HCdx} = -\frac{b}{Q_{HC}} \cdot J_{Cl} - C_{Cl,HC} \cdot \frac{b \cdot J_{H2O}}{Q_{HC}} \cdot V_{H2O}$$ Cl ions permeate from HC to LC, negative change to HC

$$C_{Na,HC} = C_{Na,HC,ini} + \int_{L_{ini}}^{L_{end}} (dC_{Na,HCdx}) \, dx$$ Dynamic change of Na in HC in respect to L

$$C_{Cl,HC} = C_{Cl,HC,ini} + \int_{L_{ini}}^{L_{end}} (dC_{Cl,HCdx}) \, dx$$ Dynamic change of Cl in HC in respect to L

$HC = HC_{ini} + C_{Na,HC} - C_{Na,HC,ini} + C_{Cl,HC} - C_{Cl,HC,ini}$ Final HC concentration [mol m^{-3}]

$$dC_{Na,LCdx} = \frac{b}{Q_{LC}} \cdot J_{Na} + C_{Na,LC} \cdot \frac{b \cdot J_{H2O}}{Q_{LC}} \cdot V_{H2O}$$ Na ions permeate from HC to LC, positive change in LC

$$dC_{Cl,LCdx} = \frac{b}{Q_{LC}} \cdot J_{Cl} + C_{Cl,LC} \cdot \frac{b \cdot J_{H2O}}{Q_{LC}} \cdot V_{H2O}$$ Cl ions permeate from HC to LC, positive change to HC

$$C_{Na,LC} = C_{Na,LC,ini} + \int_{L_{ini}}^{L_{end}} (dC_{Na,LCdx}) \, dx$$ Dynamic change of Na in LC in respect to L

$$C_{Cl,LC} = C_{Cl,LC,ini} + \int_{L_{ini}}^{L_{end}} (dC_{Cl,LCdx}) \, dx$$ Dynamic change of Cl in LC in respect to L

$LC = LC_{ini} + C_{Na,LC} - C_{Na,LC,ini} + C_{Cl,LC} - C_{Cl,LC,ini}$ Final LC concentration [mol m^{-3}]

Molality of Solution

$$m_{HC} = \frac{HC}{\rho_{water}}$$ Molality of HC bulk [mol kg^{-1}]

$$m_{LC} = \frac{LC}{\rho_{water}}$$ Molality of LC bulk [mol kg^{-1}]

$$m_{Na,HC} = \frac{C_{Na,HC}}{\rho_{water}}$$ Molality Na ions in HC [mol kg^{-1}]

$$m_{Cl,HC} = \frac{C_{Cl,HC}}{\rho_{water}}$$ Molality Cl ions in HC [mol kg^{-1}]

$$m_{Na,LC} = \frac{C_{Na,LC}}{\rho_{water}}$$ Molality Na ions in LC [mol kg^{-1}]

$$m_{Cl,LC} = \frac{C_{Cl,LC}}{\rho_{water}}$$ Molality Cl ions in LC [mol kg^{-1}]

Water Density with temp

$$\rho_{water} = \frac{1000 + 16.945176 \cdot t_C - 7.9870401 \cdot 10^{-3} \cdot t_C{}^2 - 46.170461 \cdot 10^{-6} \cdot t_C{}^3 + 105.56302 \cdot 10^{-9} \cdot t_C{}^4 - 280.54253 \cdot 10^{-12} \cdot t_C{}^5}{1 + 16.89785 \cdot 10^{-3} \cdot t_C}$$ Temperature dependent water density [kg m^{-3}]

Internal Resistance - ohmic & non-ohmic

$R_{cell} = R_{ohmic} + R_{nonohmic}$ Total resistance (ohmic & non-ohmic) in a cell pair [ohms m^{-2}]

R_{ohmic}

$R_{ohmic} = R_{AEM} + R_{CEM} + R_{cond,tot}$ Total ohmic resistance in a cell pair [ohms m^{-2}]

$$R_{HC} = \frac{\varepsilon_L}{\varepsilon^2 \cdot Cond_{HC} \cdot 10^{-4}}$$ Areal resistance of concentrate compartment, uS/cm to S/m -> 10^{-4} [Ohm m^{-2}]

$$R_{LC} = \frac{\varepsilon_L}{\varepsilon^2 \cdot Cond_{LC} \cdot 10^{-4}}$$ Areal resistance of diluate compartment, uS/cm to S/m -> 10^{-4} [Ohm m^{-2}]

$R_{cond,tot} = R_{HC} + R_{LC}$

$R_{nonohmic}$

$R_{nonohmic} = R_{\Delta C} + R_{BL,tot}$ Total non-ohmic resistance in a cell pair [ohms m^{-2}]

$$R_{\Delta C} = \frac{\alpha \cdot R \cdot T}{z_{Na} \cdot F \cdot j} \cdot \ln \left[\frac{1 + \frac{j \cdot tr_{LC}}{F \cdot \varepsilon \cdot \varepsilon_L \cdot LC}}{1 - \frac{j \cdot tr_{HC}}{F \cdot \varepsilon \cdot \varepsilon_L \cdot HC}} \right]$$ Resistance due to concentration change along flow axis in bulk solution [ohms m^{-2}]

$R_{BL,tot} = R_{BL,HC} + R_{BL,LC}$ Resistance due to diffusion boundary layer build up between the membrane interface and the fluid bulk, reducing the effective transmembrane concentration difference, and therefore the e.m.f.

$$R_{BL,HC} = 10^{-3} \cdot \left[0.62 \cdot \frac{tr_{HC} \cdot \varepsilon_L}{L} + 0.05 \right]$$ Resistance due to concentration polarisation phenomena HC [ohms m^{-2}]

$$R_{BL,LC} = 10^{-3} \cdot \left[0.62 \cdot \frac{tr_{LC} \cdot \varepsilon_L}{L} + 0.05 \right]$$ Resistance due to concentration polarisation phenomena LC [ohms m^{-2}]

Activity Coefficient Derivation - Pitzer/Weber

Mean Activity Coefficients - Pitzer model of electrolyte thermodynamics

$$\gamma_{LC} = \exp\left[-A_1 \cdot \left(\frac{\sqrt{\frac{LC}{1000}}}{1 + \dot{b} \cdot \sqrt{\frac{LC}{1000}}} + \frac{2}{b} \cdot \ln\left[1 + \dot{b} \cdot \sqrt{\frac{LC}{1000}} \right] \right) + m_{LC} \cdot B^y + m_{LC}^2 \cdot C^y \right] \quad \text{Mean activity coefficient NaCl in HC}$$

$$\gamma_{HC} = \exp\left[-A_1 \cdot \left(\frac{\sqrt{\frac{HC}{1000}}}{1 + \dot{b} \cdot \sqrt{\frac{HC}{1000}}} + \frac{2}{b} \cdot \ln\left[1 + \dot{b} \cdot \sqrt{\frac{HC}{1000}} \right] \right) + m_{HC} \cdot B_2^y + m_{HC}^2 \cdot C^y \right] \quad \text{Mean activity coefficient NaCl in LC}$$

$$\gamma_{Na,HC} = \exp\left[-A_1 \cdot \left(\frac{\sqrt{\frac{C_{Na,HC}}{1000}}}{1 + \dot{b} \cdot \sqrt{\frac{C_{Na,HC}}{1000}}} + \frac{2}{b} \cdot \ln\left[1 + \dot{b} \cdot \sqrt{\frac{C_{Na,HC}}{1000}} \right] \right) + m_{Na,HC} \cdot B_{Na,HC}^y m_{Na,HC}^2 \cdot C^y \right] \quad \text{Activity of Na in HC}$$

$$\gamma_{Cl,HC} = \exp\left[-A_1 \cdot \left(\frac{\sqrt{\frac{C_{Cl,HC}}{1000}}}{1 + \dot{b} \cdot \sqrt{\frac{C_{Cl,HC}}{1000}}} + \frac{2}{b} \cdot \ln\left[1 + \dot{b} \cdot \sqrt{\frac{C_{Cl,HC}}{1000}} \right] \right) + m_{Cl,HC} \cdot B_{Cl,HC}^y m_{Cl,HC}^2 \cdot C^y \right] \quad \text{Activity of Cl in HC}$$

$$\gamma_{Na,LC} = \exp\left[-A_1 \cdot \left(\frac{\sqrt{\frac{C_{Na,LC}}{1000}}}{1 + \dot{b} \cdot \sqrt{\frac{C_{Na,LC}}{1000}}} + \frac{2}{b} \cdot \ln\left[1 + \dot{b} \cdot \sqrt{\frac{C_{Na,LC}}{1000}} \right] \right) + m_{Na,LC} \cdot B_{Na,LC}^y m_{Na,LC}^2 \cdot C^y \right] \quad \text{Activity of Na in LC}$$

$$\gamma_{Cl,LC} = \exp\left[-A_1 \cdot \left(\frac{\sqrt{\frac{C_{Cl,LC}}{1000}}}{1 + \dot{b} \cdot \sqrt{\frac{C_{Cl,LC}}{1000}}} + \frac{2}{b} \cdot \ln\left[1 + \dot{b} \cdot \sqrt{\frac{C_{Cl,LC}}{1000}} \right] \right) + m_{Cl,LC} \cdot B_{Cl,LC}^y m_{Cl,LC}^2 \cdot C^y \right] \quad \text{Activity of Cl in LC}$$

Virial Coefficients - Pitzer system

$$B^y = 2 \cdot 0.06743 + 2 \cdot 0.3301 \cdot \frac{\left[1 - \left(1 + \alpha_2 \cdot m_{LC}^{0.5} - \alpha_2^2 \cdot \frac{m_{LC}}{2} \right) \right] \cdot \exp\left(-\alpha_2 \cdot m_{LC}^{0.5} \right)}{\alpha_2^2 \cdot m_{LC}}$$

$$B_2^y = 2 \cdot 0.06743 + 2 \cdot 0.3301 \cdot \frac{\left[1 - \left(1 + \alpha_2 \cdot m_{HC}^{0.5} - \alpha_2^2 \cdot \frac{m_{HC}}{2} \right) \right] \cdot \exp\left(-\alpha_2 \cdot m_{HC}^{0.5} \right)}{\alpha_2^2 \cdot m_{HC}}$$

$$B_{Na,HC}^y 2 \cdot 0.06743 + 2 \cdot 0.3301 \cdot \frac{\left[1 - \left(1 + \alpha_2 \cdot m_{Na,HC}^{0.5} - \alpha_2^2 \cdot \frac{m_{Na,HC}}{2} \right) \right] \cdot \exp\left(-\alpha_2 \cdot m_{Na,HC}^{0.5} \right)}{\alpha_2^2 \cdot m_{Na,HC}}$$

$$B_{Cl,HC}^y 2 \cdot 0.06743 + 2 \cdot 0.3301 \cdot \frac{\left[1 - \left(1 + \alpha_2 \cdot m_{Cl,HC}^{0.5} - \alpha_2^2 \cdot \frac{m_{Cl,HC}}{2} \right) \right] \cdot \exp\left(-\alpha_2 \cdot m_{Cl,HC}^{0.5} \right)}{\alpha_2^2 \cdot m_{Cl,HC}}$$

$$B_{Na,LC}^y 2 \cdot 0.06743 + 2 \cdot 0.3301 \cdot \frac{\left[1 - \left(1 + \alpha_2 \cdot m_{Na,LC}^{0.5} - \alpha_2^2 \cdot \frac{m_{Na,LC}}{2} \right) \right] \cdot \exp\left(-\alpha_2 \cdot m_{Na,LC}^{0.5} \right)}{\alpha_2^2 \cdot m_{Na,LC}}$$

$$B_{Cl,LC}^y 2 \cdot 0.06743 + 2 \cdot 0.3301 \cdot \frac{\left[1 - \left(1 + \alpha_2 \cdot m_{Cl,LC}^{0.5} - \alpha_2^2 \cdot \frac{m_{Cl,LC}}{2} \right) \right] \cdot \exp\left(-\alpha_2 \cdot m_{Cl,LC}^{0.5} \right)}{\alpha_2^2 \cdot m_{Cl,LC}}$$

$\alpha_2 = 2$

$A_1 = 0.3215$

$\dot{b} = 1.2$

$C^y = 3 / 2 \cdot 0.00263$

Conductivity

$$LCEC_{25} = \frac{F^2}{R \cdot T} \cdot (0.0133 + 0.0203) \cdot z_{Na}^2 \cdot \gamma_{LC}^{\alpha_3} \cdot \frac{LC}{1000} \quad \text{EC at 25C in LC [uS cm}^{-1}\text{]}$$

$$HCEC_{25} = \frac{F^2}{R \cdot T} \cdot (0.0133 + 0.0203) \cdot z_{Na}^2 \cdot \gamma_{HC}^{\alpha_4} \cdot \frac{HC}{1000} \quad \text{EC at 25C in HC [uS cm}^{-1}\text{]}$$

IfTest $(LC) = \alpha_3$ Appelo parametrisation for LC

$$\alpha_4 = \left[\frac{HC}{1000} \right]^{0.5} \quad \text{Appelo parametrisation for HC}$$

$$Cond_{LC} = 0.889 \cdot 10^{\left[\frac{A_c}{B_c} \right]} \cdot LCEC_{25} \quad \text{Temperature dependent EC of LC}$$

$$Cond_{HC} = 0.889 \cdot 10^{\left[\frac{A_c}{B_c} \right]} \cdot HCEC_{25} \quad \text{Temperature dependent EC HC}$$

Temperature correlation

$$A_c = 1.37023 \cdot (t_C - 20) + 8.36 \cdot 10^{-4} \cdot (t_C - 20)^2$$

$$B_c = 109 + t_C$$

Mole Fractions

$$Mass_{solvent} = \frac{\rho_{water}}{1000} \quad \text{Mass in kg of 1L water}$$

$$Mol_{solvent} = \frac{Mass_{solvent}}{M_{H2O}} \quad \text{Mass/(molecular weight in kg/mol) = mols of solvent}$$

$$Mol_{HC} = \frac{HC}{1000} \quad \text{HC in mol/L}$$

$$Mol_{LC} = \frac{LC}{1000} \quad \text{LC in mol/L}$$

$$\chi_{H2O,HC} = \frac{Mol_{solvent}}{Mol_{solvent} + Mol_{HC}}$$ Mole fraction of water in HC solution

$$\chi_{NaCl,HC} = \frac{Mol_{HC}}{Mol_{solvent} + Mol_{HC}}$$ Mole fraction of NaCl in HC

$$\chi_{HC} = \chi_{H2O,HC} + \chi_{NaCl,HC} \quad = 1$$

$$\chi_{H2O,LC} = \frac{Mol_{solvent}}{Mol_{solvent} + Mol_{LC}}$$ Mole fraction of water in LC solution

$$\chi_{NaCl,LC} = \frac{Mol_{LC}}{Mol_{solvent} + Mol_{LC}}$$ Mole fraction of NaCl in LC

$$\chi_{LC} = \chi_{H2O,LC} + \chi_{NaCl,LC} \quad = 1$$

$$V_{m,NaCl,HC} = 1.514218 \cdot 10^{-5} + 2.528718 \cdot 10^{-5} \cdot \left[\frac{\sqrt{\chi_{NaCl,HC}}}{1 + \sqrt{\chi_{NaCl,HC}}} \right]$$

$$V_{m,NaCl,LC} = 1.514218 \cdot 10^{-5} + 2.528718 \cdot 10^{-5} \cdot \left[\frac{\sqrt{\chi_{NaCl,LC}}}{1 + \sqrt{\chi_{NaCl,LC}}} \right]$$

$$V_{m,HC} = \chi_{H2O,HC} \cdot V_{H2O} + \chi_{NaCl,HC} \cdot V_{m,NaCl,HC}$$ Apparent molar volume of HC electrolyte [m^3 mol^{-1}]

$$V_{m,LC} = \chi_{H2O,LC} \cdot V_{H2O} + \chi_{NaCl,LC} \cdot V_{m,NaCl,LC}$$ Apparent molar volume of LC electrolyte [m^3 mol^{-1}]

$$C_{HC} = \frac{\chi_{NaCl,HC}}{V_{m,HC}}$$

$$C_{LC} = \frac{\chi_{NaCl,LC}}{V_{m,LC}}$$

Viscosity

$$\mu_w = \exp\left[-45.9352 + \frac{3703.6}{T} + 5.866 \cdot \ln(T) - 0.5879 \cdot 10^{-28} \cdot T^{10} \right]$$ Temp dependent viscosity of pure water

$$\mu_{ca,Na,LC} = 0.005011 \cdot \sqrt{\frac{LC}{1000}} + 0.0863 \cdot \frac{C_{LC}}{1000}$$

$$\mu_{ca,Cl,LC} = 0.007634 \cdot \sqrt{\frac{LC}{1000}} + -0.007 \cdot \frac{C_{LC}}{1000}$$

$$\mu_{LC} = \mu_w \cdot \left[\frac{1 + \mu_{ca,Na,LC} + \mu_{ca,Cl,LC}}{1000} \right]$$ Viscosity of LC soln, MPa*S. Divided by 1000 for MPa -> Pa

$$\mu_{ca,Na,HC} = 25 \cdot V_{e,Na} \cdot \frac{C_{HC}}{1000} + 105 \cdot V_{e,Na} \cdot \left[\frac{C_{HC}}{1000} \right]^2$$

$$\mu_{Ca,Cl,HC} = 25 \cdot V_{e,Cl} \cdot \frac{C_{HC}}{1000} + 105 \cdot V_{e,Cl} \cdot \left[\frac{C_{HC}}{1000} \right]^2$$

$$V_{e,Na} = \frac{0.0863 - 0.002}{260}$$

$$V_{e,Cl} = \frac{-0.007 - 0.002}{260}$$

$$\mu_{HC} = \frac{\mu_w \cdot (1 + \mu_{ca,Na,HC} + \mu_{Ca,Cl,HC})}{1000}$$ viscosity of HC soln [MPa S]. Divided by 1000 for MPa -> Pa

Pumps

$$dP_{HCdx} = -\frac{48 \cdot \mu_{HC} \cdot Q_{HC}}{D_h^2 \cdot b \cdot \varepsilon_L \cdot \varepsilon}$$ Pressure drop rate in HC [Pa]

$$dP_{LCdx} = -\frac{48 \cdot \mu_{LC} \cdot Q_{LC}}{D_h^2 \cdot b \cdot \varepsilon_L \cdot \varepsilon}$$ Pressure drop rate in LC [Pa]

$$D_h = \frac{4 \cdot \varepsilon}{\frac{2}{\varepsilon_L} + (1 - \varepsilon) \cdot \frac{8}{\varepsilon_L}}$$ Hydraulic diameter of a compartment - Assumed same in HC & LC

$$Pressure_{drop,HC,avg} = \frac{\int_{L_{ini}}^{L_{end}} (dP_{HCdx}) \, dx}{\int_{L_{ini}}^{L_{end}} (x) \, dx + 1.0 \times 10^{-9}}$$

$$Pressure_{drop,LC,avg} = \frac{\int_{L_{ini}}^{L_{end}} (dP_{LCdx}) \, dx}{\int_{L_{ini}}^{L_{end}} (x) \, dx + 1.0 \times 10^{-9}}$$

$$P_{pump} = \frac{Q_{HC,ini} \cdot Pressure_{drop,HC,avg} + Q_{LC,ini} \cdot Pressure_{drop,LC,avg}}{0.75}$$ Pumping power required for design flow rate [W]

8.0 REFERENCES

Achilli, A., Prante, J. L., Hancock, N. T., Maxwell, E. B., & Childress, A. E. (2014). Experimental results from RO-PRO: a next generation system for low-energy desalination. *Environmental Science & Technology*, *48*(11), 6437-6443.

Agre, P. (2006). The aquaporin water channels. *Proceedings of the American Thoracic Society*, *3*(1), 5-13.

Allison, R. P. (1995). Electrodialysis reversal in water reuse applications. *Desalination*, *103*(1-2), 11-18.

Alvarez-Silva, O., Osorio, A. F., & Winter, C. (2016). Practical global salinity gradient energy potential. *Renewable and Sustainable Energy Reviews*, *60*, 1387-1395.

Amy, G., Ghaffour, N., Li, Z., Francis, L., Linares, R. V., Missimer, T., & Lattemann, S. (2017). Membrane-based seawater desalination: Present and future prospects. *Desalination*, *401*, 16-21.

Appelo, C. (2017). Solute transport solved with the Nernst-Planck equation for concrete pores with 'free'water and a double layer. *Cement and Concrete Research*, *101*, 102-113.

aqion. (2021). *Temperature Compensation for Conductivity*. https://www.aqion.de/site/112#fn:1

Atkins, P., & De Paula, J. (2011). *Physical chemistry for the life sciences*. Oxford University Press, USA.

Audinos, R. (1983). Reverse electrodialysis. Study of the electric energy obtained by mixing two solutions of different salinity. *Journal of Power Sources*, *10*(3), 203-217.

Audinos, R. (1992). Electric power produced from two solutions of unequal salinity by reverse electrodialysis.

Authority, E. P. (2009). Perth Metropolitan Desalination Proposal–Water Quality Management, Change to Implementation Conditions.

Avrotros. (2019). *Blauw is het nieuwe groen*. https://www.youtube.com/watch?app=desktop&v=W31CTzVGzYY&t=20s

Balomenos, E., Panias, D., & Paspaliaris, I. (2006). Modeling chemical equilibrium of electrolyte solutions. *Mineral Processing and Extractive Metallurgy Review*, *27*(1), 1-60.

Beaudry, E. G., Herron, J. R., & Peterson, S. (1999). Direct osmosis concentration of waste water: Final report. *Osmotek Inc., Corvallis, OR*.

Benneker, A. M., Rijnaarts, T., Lammertink, R. G., & Wood, J. A. (2018). Effect of temperature gradients in (reverse) electrodialysis in the Ohmic regime. *Journal of Membrane Science*, *548*, 421-428.

Brauns, E. (2009). Salinity gradient power by reverse electrodialysis: effect of model parameters on electrical power output. *Desalination*, *237*(1-3), 378-391.

Charcosset, C., Falconet, C., & Combe, M. (2009). Hydrostatic pressure plants for desalination via reverse osmosis. *Renewable energy*, *34*(12), 2878-2882.

Chung, T.-S., Zhang, S., Wang, K. Y., Su, J., & Ling, M. M. (2012). Forward osmosis processes: yesterday, today and tomorrow. *Desalination*, *287*, 78-81.

Cipollina, A., Misseri, A., Staiti, G. D. A., Galia, A., Micale, G., & Scialdone, O. (2012). Integrated production of fresh water, sea salt and magnesium from sea water. *Desalination and Water Treatment*, *49*(1-3), 390-403.

Culcasi, A., Gurreri, L., Zaffora, A., Cosenza, A., Tamburini, A., Cipollina, A., & Micale, G. (2020). Ionic shortcut currents via manifolds in reverse electrodialysis stacks. *Desalination*, *485*, 114450.

Daniilidis, A., Herber, R., & Vermaas, D. A. (2014). Upscale potential and financial feasibility of a reverse electrodialysis power plant. *Applied Energy*, *119*, 257-265.

Długołęcki, P., Dąbrowska, J., Nijmeijer, K., & Wessling, M. (2010). Ion conductive spacers for increased power generation in reverse electrodialysis. *Journal of Membrane Science*, *347*(1-2), 101-107.

Elimelech, M., & Phillip, W. A. (2011). The future of seawater desalination: energy, technology, and the environment. *science*, *333*(6043), 712-717.

Ghaffour, N. (2009). The challenge of capacity-building strategies and perspectives for desalination for sustainable water use in MENA. *Desalination and Water Treatment*, *5*(1-3), 48-53.

Ghaffour, N., Missimer, T. M., & Amy, G. L. (2013). Technical review and evaluation of the economics of water desalination: current and future challenges for better water supply sustainability. *Desalination*, *309*, 197-207.

Giacalone, F., Catrini, P., Tamburini, A., Cipollina, A., Piacentino, A., & Micale, G. (2018). Exergy analysis of reverse electrodialysis. *Energy Conversion and Management*, *164*, 588-602.

Giacalone, F., Vassallo, F., Griffin, L., Ferrari, M.-C., Micale, G., Scargiali, F., Tamburini, A., & Cipollina, A. (2019). Thermolytic reverse electrodialysis heat engine: model development, integration and performance analysis. *Energy Conversion and Management*, *189*, 1-13.

Gómez-Coma, L., Ortiz-Martínez, V. M., Carmona, J., Palacio, L., Prádanos, P., Fallanza, M., Ortiz, A., Ibañez, R., & Ortiz, I. (2019). Modeling the influence of divalent ions on membrane resistance and electric power in reverse electrodialysis. *Journal of Membrane Science*, *592*, 117385.

Gurreri, L., Tamburini, A., Cipollina, A., Micale, G., & Ciofalo, M. (2016). Flow and mass transfer in spacer-filled channels for reverse electrodialysis: a CFD parametrical study. *Journal of Membrane Science*, *497*, 300-317.

Hakkenes, E. (2017). *Polderkoorts: hoe de Zuiderzee verdween*. De Bezige Bij.

Hayashi, M. (2004). Temperature-electrical conductivity relation of water for environmental monitoring and geophysical data inversion. *Environmental monitoring and assessment*, *96*(1), 119-128.

Helfer, F., Sahin, O., Lemckert, C., & Anissimov, Y. G. (2013). Salinity gradient energy: a new source of renewable energy for Australia. 8th International Conference of the European Water Resources Association,

Hofste, R. W., Kuzma, S., Walker, S., Sutanudjaja, E. H., Bierkens, M. F., Kuijper, M. J., Sanchez, M. F., Van Beek, R., Wada, Y., & Rodríguez, S. G. (2019). Aqueduct 3.0: Updated decision-relevant global water risk indicators. *World Resources Institute: Washington, DC, USA*.

Hong, J. G., Zhang, B., Glabman, S., Uzal, N., Dou, X., Zhang, H., Wei, X., & Chen, Y. (2015). Potential ion exchange membranes and system performance in reverse electrodialysis for power generation: A review. *Journal of Membrane Science*, *486*, 71-88.

Hong, J. G., Zhang, W., Luo, J., & Chen, Y. (2013). Modeling of power generation from the mixing of simulated saline and freshwater with a reverse electrodialysis system: The effect of monovalent and multivalent ions. *Applied Energy*, *110*, 244-251.

Hsu, J.-P., Lin, S.-C., Lin, C.-Y., & Tseng, S. (2017). Power generation by a pH-regulated conical nanopore through reverse electrodialysis. *Journal of Power Sources*, *366*, 169-177.

Hwang, J., Sekimoto, T., Hsu, W.-L., Kataoka, S., Endo, A., & Daiguji, H. (2017). Thermal dependence of nanofluidic energy conversion by reverse electrodialysis. *Nanoscale*, *9*(33), 12068-12076.

Isaacs, J. D., & Schmitt, W. R. (1980). Ocean energy: forms and prospects. *science*, *207*(4428), 265-273.

Jagur-Grodzinski, J., & Kramer, R. (1986). Novel process for direct conversion of free energy of mixing into electric power. *Industrial & Engineering Chemistry Process Design and Development*, *25*(2), 443-449.

Jin, D., Xi, R., Xu, S., Wang, P., & Wu, X. (2021). Numerical simulation of salinity gradient power generation using reverse electrodialysis. *Desalination*, *512*, 115132.

Jones, A., & Finley, W. (2003). Recent development in salinity gradient power. Oceans 2003. Celebrating the Past... Teaming Toward the Future (IEEE Cat. No. 03CH37492),

Jones, E., Qadir, M., van Vliet, M. T., Smakhtin, V., & Kang, S.-m. (2019). The state of desalination and brine production: A global outlook. *Science of the Total Environment*, *657*, 1343-1356.

Jones, F. E., & Harris, G. L. (1992). ITS-90 density of water formulation for volumetric standards calibration. *Journal of research of the National Institute of Standards and Technology*, *97*(3), 335.

Kamcev, J., Sujanani, R., Jang, E.-S., Yan, N., Moe, N., Paul, D. R., & Freeman, B. D. (2018). Salt concentration dependence of ionic conductivity in ion exchange membranes. *Journal of Membrane Science*, *547*, 123-133.

Katz, W. E. (1979). The electrodialysis reversal (EDR) process. *Desalination*, *28*(1), 31-40.

Kempener, R., & Neumann, F. (2014). Wave energy technology brief. *International Renewable Energy Agency (IRENA)*.

Khatibi, M., Sadeghi, A., & Ashrafizadeh, S. N. (2021). Tripling the reverse electrodialysis power generation in conical nanochannels utilizing soft surfaces. *Physical Chemistry Chemical Physics*, *23*(3), 2211-2221.

Kim, J., Park, K., Yang, D. R., & Hong, S. (2019). A comprehensive review of energy consumption of seawater reverse osmosis desalination plants. *Applied Energy*, *254*, 113652.

Kniajev, V. (2001). Energy of salinity gradient-new source of energy with minimal environmental impact. International Workshop "Result of Fundamental Research for Investments"(IWRFRI'2001'), St. Petersburg. Russia,

Kuleszo, J., Kroeze, C., Post, J., & Fekete, B. M. (2010). The potential of blue energy for reducing emissions of CO2 and non-CO2 greenhouse gases. *Journal of Integrative Environmental Sciences*, *7*(S1), 89-96.

Lacey, R. (1980). Energy by reverse electrodialysis. *Ocean engineering*, *7*(1), 1-47.

Li, X., & Yang, H. Y. (2021). A Global Challenge: Clean Drinking Water. *Global Challenges*, *5*(1).

Logan, B. E., & Elimelech, M. (2012). Membrane-based processes for sustainable power generation using water. *Nature*, *488*(7411), 313-319.

McCleskey, R. B., Nordstrom, D. K., & Ryan, J. N. (2012). Comparison of electrical conductivity calculation methods for natural waters. *Limnology and Oceanography: Methods*, *10*(11), 952-967.

McGovern, R. K. (2014). On the potential of forward osmosis to energetically outperform reverse osmosis desalination. *Journal of Membrane Science*, *469*, 245-250.

Mehdizadeh, S., Yasukawa, M., Abo, T., Kuno, M., Noguchi, Y., & Higa, M. (2019). The effect of feed solution temperature on the power output performance of a pilot-scale reverse electrodialysis (RED) system with different intermediate distance. *Membranes*, *9*(6), 73.

Mei, Y., & Tang, C. Y. (2018). Recent developments and future perspectives of reverse electrodialysis technology: A review. *Desalination*, *425*, 156-174.

Mekonnen, M. M., & Hoekstra, A. Y. (2016). Four billion people facing severe water scarcity. *Science advances*, *2*(2), e1500323.

Merz, C. R., Moreno, W. A., Barger, M., & Lipka, S. M. (2012). Salinity gradient power (SGP): A developmental roadmap covering existing generation technologies and recent investigative results into the feasibility of bipolar membrane-based salinity gradient power generation. *Technology & Innovation*, *14*(3-4), 249-275.

Mickley, M., Voutchkov, N., & Alexandria, V. (2016). Desal-13-07 Database of Permitting Practices for Seawater Concentrate Disposal.

Miller, R. L., Bradford, W. L., & Peters, N. E. (1988). *Specific conductance: theoretical considerations and application to analytical quality control* (Vol. 142). US Government Printing Office.

Moreno, J., Grasman, S., van Engelen, R., & Nijmeijer, K. (2018). Upscaling reverse electrodialysis. *Environmental Science & Technology*, *52*(18), 10856-10863.

Nassrullah, H., Anis, S. F., Hashaikeh, R., & Hilal, N. (2020). Energy for desalination: A state-of-the-art review. *Desalination*, *491*, 114569.

Neumann, F. (2012). Report of the meeting on salinity gradient power generation. *Institute for Infrastructure, Environment and Innovation (IMI): Brussels, Belgium*, 1-61.

Ortega-Delgado, B., Giacalone, F., Cipollina, A., Papapetrou, M., Kosmadakis, G., Tamburini, A., & Micale, G. (2019). Boosting the performance of a Reverse Electrodialysis–Multi-Effect

Distillation Heat Engine by novel solutions and operating conditions. *Applied Energy*, *253*, 113489.

Ortiz-Imedio, R., Gomez-Coma, L., Fallanza, M., Ortiz, A., Ibañez, R., & Ortiz, I. (2019). Comparative performance of Salinity Gradient Power-Reverse Electrodialysis under different operating conditions. *Desalination*, *457*, 8-21.

Park, J.-S., Choi, J.-H., Woo, J.-J., & Moon, S.-H. (2006). An electrical impedance spectroscopic (EIS) study on transport characteristics of ion-exchange membrane systems. *Journal of colloid and interface science*, *300*(2), 655-662.

Park, K., Heo, H., & Yang, D. R. (2018). Feasibility study of a forward osmosis/crystallization/reverse osmosis hybrid process with high-temperature operation: Modeling, experiments, and energy consumption. *Journal of Membrane Science*, *555*, 206-219.

Pattle, R. (1954). Production of electric power by mixing fresh and salt water in the hydroelectric pile. *Nature*, *174*(4431), 660-660.

Pattle, R. (1955). Improvements to electric batteries. *Patent GB*, *731729*.

Pawlowski, S., Crespo, J., & Velizarov, S. (2016). Sustainable power generation from salinity gradient energy by reverse electrodialysis. In *Electrokinetics Across Disciplines and Continents* (pp. 57-80). Springer.

Pitzer, K. S. (1973). Thermodynamics of electrolytes. I. Theoretical basis and general equations. *The Journal of Physical Chemistry*, *77*(2), 268-277.

Post, J. W., Hamelers, H. V., & Buisman, C. J. (2008). Energy recovery from controlled mixing salt and fresh water with a reverse electrodialysis system. *Environmental Science & Technology*, *42*(15), 5785-5790.

Post, J. W., Veerman, J., Hamelers, H. V., Euverink, G. J., Metz, S. J., Nymeijer, K., & Buisman, C. J. (2007). Salinity-gradient power: Evaluation of pressure-retarded osmosis and reverse electrodialysis. *Journal of Membrane Science*, *288*(1-2), 218-230.

Quak, R. (2009). Feasibility of a power plant: Blue energy in the Dutch Delta.

Rabiee, H., Khalilpour, K. R., Betts, J. M., & Tapper, N. (2019). Energy-water nexus: renewable-integrated hybridized desalination systems. *Polygeneration with polystorage for chemical and energy hubs*, 409-458.

Ramanathan, V., & Feng, Y. (2009). Air pollution, greenhouse gases and climate change: Global and regional perspectives. *Atmospheric environment*, *43*(1), 37-50.

Ramon, G. Z., Feinberg, B. J., & Hoek, E. M. (2011). Membrane-based production of salinity-gradient power. *Energy & environmental science*, *4*(11), 4423-4434.

REAPower. (2014). *Reverse Electrodialysis Technology*. https://www.reapower.eu/project-scope/reverse-electrodyalisis-technology.html

REDstack. (2016). *SALINITY GRADIENT ENERGY WORLDWIDE POTENTIAL*. https://redstack.nl/wp-content/uploads/2021/02/NWP-worldmap-Salinity-Gradient-Energy.pdf

Robinson, R., & Stokes, R. (1959). Electrolyte Solutions, Butterworths Scientific Publications. *London. 2nd editi on*.

Sanz, M. A., Stover, R. L., & Degrémont, S. (2007). Low energy consumption in the Perth seawater desalination plant. IDA World Congress–Maspalomas, Gran Canaria, Spain,

Schiermeier, Q. (2008). Water: purification with a pinch of salt. In: Nature Publishing Group.

Scialdone, O., Guarisco, C., Grispo, S., D'Angelo, A., & Galia, A. (2012). Investigation of electrode material–Redox couple systems for reverse electrodialysis processes. Part I: Iron redox couples. *Journal of Electroanalytical Chemistry*, *681*, 66-75.

Shahzad, M. W., Burhan, M., Ang, L., & Ng, K. C. (2017). Energy-water-environment nexus underpinning future desalination sustainability. *Desalination*, *413*, 52-64.

Skilhagen, S. E., Dugstad, J. E., & Aaberg, R. J. (2008). Osmotic power—power production based on the osmotic pressure difference between waters with varying salt gradients. *Desalination*, *220*(1-3), 476-482.

Staples, B. R. (1981). Activity and osmotic coefficients of aqueous alkali metal nitrites. *Journal of Physical and Chemical Reference Data*, *10*(3), 765-778.

Stover, R. L. (2007). Seawater reverse osmosis with isobaric energy recovery devices. *Desalination*, *203*(1-3), 168-175.

Strathmann, H. (2010). Electrodialysis, a mature technology with a multitude of new applications. *Desalination*, *264*(3), 268-288.

Suda, F., Matsuo, T., & Ushioda, D. (2007). Transient changes in the power output from the concentration difference cell (dialytic battery) between seawater and river water. *Energy*, *32*(3), 165-173.

Tamburini, A., Cipollina, A., Papapetrou, M., Piacentino, A., & Micale, G. (2016). Salinity gradient engines. In *Sustainable energy from salinity gradients* (pp. 219-256). Elsevier.

Tedesco, M., Cipollina, A., Tamburini, A., Bogle, I. D. L., & Micale, G. (2015). A simulation tool for analysis and design of reverse electrodialysis using concentrated brines. *Chemical Engineering Research and Design*, *93*, 441-456.

Tedesco, M., Cipollina, A., Tamburini, A., & Micale, G. (2017). Towards 1 kW power production in a reverse electrodialysis pilot plant with saline waters and concentrated brines. *Journal of Membrane Science*, *522*, 226-236.

Tedesco, M., Hamelers, H., & Biesheuvel, P. (2016). Nernst-Planck transport theory for (reverse) electrodialysis: I. Effect of co-ion transport through the membranes. *Journal of Membrane Science*, *510*, 370-381.

Tedesco, M., Scalici, C., Vaccari, D., Cipollina, A., Tamburini, A., & Micale, G. (2016). Performance of the first reverse electrodialysis pilot plant for power production from saline waters and concentrated brines. *Journal of Membrane Science*, *500*, 33-45.

Telesh, I. V., & Khlebovich, V. V. (2010). Principal processes within the estuarine salinity gradient: a review. *Marine Pollution Bulletin*, *61*(4-6), 149-155.

Thomson, G. (1996). The DIPPR® databases. *International journal of thermophysics*, *17*(1), 223-232.

Tristán, C., Fallanza, M., Ibáñez, R., & Ortiz, I. (2020). Recovery of salinity gradient energy in desalination plants by reverse electrodialysis. *Desalination*, *496*, 114699.

Tufa, R. A., Curcio, E., Brauns, E., van Baak, W., Fontananova, E., & Di Profio, G. (2015). Membrane distillation and reverse electrodialysis for near-zero liquid discharge and low energy seawater desalination. *Journal of Membrane Science*, *496*, 325-333.

Tufa, R. A., Curcio, E., van Baak, W., Veerman, J., Grasman, S., Fontananova, E., & Di Profio, G. (2014). Potential of brackish water and brine for energy generation by salinity gradient power-reverse electrodialysis (SGP-RE). *RSC Advances*, *4*(80), 42617-42623.

Turek, M., & Bandura, B. (2007). Renewable energy by reverse electrodialysis. *Desalination*, *205*(1-3), 67-74.

United Nations. (2015). *Goal 6: Ensure access to water and sanitation for all*. https://unric.org/en/sdg-6/

van Vliet, M. T., Jones, E. R., Flörke, M., Franssen, W. H., Hanasaki, N., Wada, Y., & Yearsley, J. R. (2021). Global water scarcity including surface water quality and expansions of clean water technologies. *Environmental Research Letters*, *16*(2), 024020.

Vanoppen, M., Blandin, G., Derese, S., Le Clech, P., Post, J., & Verliefde, A. R. D. (2016). 9 - Salinity gradient power and desalination. In (pp. 281-313). Elsevier Ltd. https://doi.org/10.1016/B978-0-08-100312-1.00009-2

Vanýsek, P. (1992). *Ionic conductivity and diffusion at infinite dilution* (Vol. 1992/93 edition). CRC Press, Boca Raton.

Veerman, J., De Jong, R., Saakes, M., Metz, S., & Harmsen, G. (2009). Reverse electrodialysis: Comparison of six commercial membrane pairs on the thermodynamic efficiency and power density. *Journal of Membrane Science*, *343*(1-2), 7-15.

Veerman, J., Post, J., Saakes, M., Metz, S., & Harmsen, G. (2008). Reducing power losses caused by ionic shortcut currents in reverse electrodialysis stacks by a validated model. *Journal of Membrane Science*, *310*(1-2), 418-430.

Veerman, J., Saakes, M., Metz, S., & Harmsen, G. (2011). Reverse electrodialysis: A validated process model for design and optimization. *Chemical Engineering Journal*, *166*(1), 256-268.

Veerman, J., Saakes, M., Metz, S. J., & Harmsen, G. (2010). Reverse electrodialysis: evaluation of suitable electrode systems. *Journal of Applied Electrochemistry*, *40*(8), 1461-1474.

Verbeke, R., Gomez, V., & Vankelecom, I. F. (2017). Chlorine-resistance of reverse osmosis (RO) polyamide membranes. *Progress in Polymer Science*, *72*, 1-15.

Vermaas, D. A., Guler, E., Saakes, M., & Nijmeijer, K. (2012). Theoretical power density from salinity gradients using reverse electrodialysis. *Energy Procedia*, *20*, 170-184.

Vermaas, D. A., Saakes, M., & Nijmeijer, K. (2011a). Doubled power density from salinity gradients at reduced intermembrane distance. *Environmental Science & Technology*, *45*(16), 7089-7095.

Vermaas, D. A., Saakes, M., & Nijmeijer, K. (2011b). Power generation using profiled membranes in reverse electrodialysis. *Journal of Membrane Science*, *385*, 234-242.

Vermaas, D. A., Saakes, M., & Nijmeijer, K. (2014). Enhanced mixing in the diffusive boundary layer for energy generation in reverse electrodialysis. *Journal of Membrane Science*, *453*, 312-319.

Voutchkov, N. (2018). Energy use for membrane seawater desalination–current status and trends. *Desalination*, *431*, 2-14.

Voutchkov, N., & Semiat, R. (2008). Seawater desalination. *Advanced membrane technology and applications*, 47-86.

Wa'el A, H., Memon, F. A., & Savic, D. A. (2018). A risk-based assessment of the household water-energy-food nexus under the impact of seasonal variability. *Journal of cleaner production*, *171*, 1275-1289.

Wakeel, M., Chen, B., Hayat, T., Alsaedi, A., & Ahmad, B. (2016). Energy consumption for water use cycles in different countries: A review. *Applied Energy*, *178*, 868-885.

Weber, C. F. (2000). Calculation of Pitzer parameters at high ionic strengths. *Industrial & engineering chemistry research*, *39*(11), 4422-4426.

Weinstein, J. N., & Leitz, F. B. (1976). Electric power from differences in salinity: the dialytic battery. *science*, *191*(4227), 557-559.

Yadav, P. S. B. (2013). *12th Std Chemistry*. Target PUBLICATIONS PVT. LTD. https://www.brainkart.com/article/Variation-of-molar-conductivity-with-concentration_41313/

Yoon, J., Do, V. Q., Pham, V.-S., & Han, J. (2019). Return flow ion concentration polarization desalination: A new way to enhance electromembrane desalination. *Water research*, *159*, 501-510.

Younos, T. (2005). Environmental issues of desalination. *Journal of contemporary water research and education*, *132*(1), 3.

Zhu, X., He, W., & Logan, B. E. (2015). Reducing pumping energy by using different flow rates of high and low concentration solutions in reverse electrodialysis cells. *Journal of Membrane Science*, *486*, 215-221.

Zlotorowicz, A., Strand, R. V., Burheim, O. S., Wilhelmsen, Ø., & Kjelstrup, S. (2017). The permselectivity and water transference number of ion exchange membranes in reverse electrodialysis. *Journal of Membrane Science*, *523*, 402-408.

Zoungrana, A., & Çakmakci, M. (2021). From non-renewable energy to renewable by harvesting salinity gradient power by reverse electrodialysis: A review. *International Journal of Energy Research*, *45*(3), 3495-3522.